

## DYNAMICAL COLLAPSE IN W51 MASSIVE CORES: CS (3–2) AND CH<sub>3</sub>CN OBSERVATIONS

QIZHOU ZHANG,<sup>1</sup> PAUL T. P. HO, AND NAGAYOSHI OHASHI<sup>2</sup>

Harvard-Smithsonian Center for Astrophysics, 60 Garden Street, Cambridge, MA 02138

Received 1997 July 24; accepted 1997 October 1

### ABSTRACT

We present interferometric observations of the W51 region at 2 mm with the Nobeyama Millimeter Array. The 320 MHz band centered at 147 GHz covers transitions of the CS (3–2), CH<sub>3</sub>CN (8–7), H35 $\alpha$ , CH<sub>3</sub>OCH<sub>3</sub> (7–6) and (6–6), and HCOOCH<sub>3</sub> (12–11), as well as the 2 mm continuum. Toward two dense cores, W51e2 and W51e8, spectroscopic signatures of cloud collapse are present in all the molecular lines observed. Line asymmetries increase systematically toward transitions of larger optical depths, consistent with expected signatures of a centrally condensed infalling cloud. Furthermore, the disparity between the blueshifted and the redshifted emission of the CS line is enhanced when the line is synthesized at higher angular resolution. Given that the continuum source is embedded in the core, we are able to locate the emitting gas of the blueshifted emission on the rear side and the gas of the redshifted emission on the front side of the central star. The new observations confirm our infall interpretations regarding the e2 and e8 cores based on the NH<sub>3</sub> data.

The compact CH<sub>3</sub>CN emission allows us to identify velocity gradients in the e2 and e8 cores. The gradient in the e2 core is consistent with the spin-up motions proposed by Zhang & Ho in 1997.

CH<sub>3</sub>CN emission reveals hot components in the W51e2, W51e8, and W51-North:dust cores. The rotational temperature in each core is greater than 100 K.

In W51-North, we detected a dust peak coincident with the peak of the dense molecular core. There is no 3.6 cm continuum detected at a level of less than 1 mJy. Although H<sub>2</sub>O and OH masers in the neighborhood indicate outflow activities, high-velocity gas is not apparent in the CS (3–2). This source may represent an extremely early evolutionary stage: the phase of massive protostars.

*Subject headings:* H II regions — ISM: clouds — ISM: individual (W51) — ISM: kinematics and dynamics — stars: formation

### 1. INTRODUCTION

W51 is an H II region complex in the Sagittarius spiral arm about 7–8 kpc away (see Bieging 1975 for a summary of early studies). In NH<sub>3</sub> and HCO<sup>+</sup>, there are three dense molecular cores identified in the 1' region (Ho, Genzel, & Das 1983; Rudolph et al. 1990). Associated with ultracompact H II (UC H II) regions and H<sub>2</sub>O, OH maser activities (Scott 1978; Gaume, Johnston, & Wilson 1993; Genzel & Downes 1977; Gaume & Mutel 1987), these cores harbor the ongoing massive star formation.

Toward the molecular cores associated with the UC H II regions W51e2 and W51e8, we found compelling spectroscopic evidence for gravitational infall (Ho & Young 1996; Zhang & Ho 1997). The optically thick NH<sub>3</sub> lines exhibit inverse P Cygni or asymmetric line profiles, consistent with the characteristics of infall. In addition, the velocity pattern across the e2 core agrees well with the expected signatures from the radial infall of a spherical cloud. A velocity gradient exists in the e2 core at scales of less than 0".4. The angular velocity increases inward as  $r^{-1}$ , indicating a spin-up of material during the course of collapse.

The W51 region, like other high-mass, star-forming regions, is located at a sufficiently large distance that complex kinematic processes are difficult to resolve spatially. To further test the infall hypothesis, we imaged the emission from a number of high-density tracers at 2 mm wavelength with the Nobeyama Millimeter Array. The 320

MHz band covered the CS (3–2), CH<sub>3</sub>CN (8–7), H35 $\alpha$ , CH<sub>3</sub>OCH<sub>3</sub> (7–6) and (6–6), and HCOOCH<sub>3</sub> (12–11) lines. The new data show infall asymmetries that are consistent with previous NH<sub>3</sub> observations. We detected velocity gradient toward the e2 core at greater than 1" scale, confirming rotation and spin-up suggested by Zhang & Ho (1997). In addition, we detected a 2 mm dust continuum peak coincident with the peak of the W51-North core. This source, without the counterpart at centimeter wavelengths, may represent an extremely young example of massive stars.

### 2. OBSERVATIONS

The W51 region was observed with the 2 mm SIS receivers of the six-element Nobeyama Millimeter Array (NMA) from 1995 December through 1996 February. Two 8 hour tracks were obtained in each of the most compact (designated D), the intermediate (C), and the most extended (AB) configurations. The projected antenna baselines range from 10 to 365 m, yielding a maximum resolution of  $\sim 1''$  when uniform weighting is applied to all the visibility data. At 147 GHz, the primary beam of the 10 m telescopes is about 45". Hence, in order to cover the W51e1/W51e2 region and the W51-North region, which are more than 1' apart, two fields were observed. The phase centers were  $\alpha(1950) = 19^{\text{h}}21^{\text{m}}26^{\text{s}}.2$  and  $\delta(1950) = 14^{\circ}24'38''$  for the e1/e2 region and  $\alpha(1950) = 19^{\text{h}}21^{\text{m}}22^{\text{s}}.16$  and  $\delta(1950) = 14^{\circ}25'11''.9$  for W51-North. The W51-North region was observed in the D and C configurations only, giving a maximum resolution of about 2". Details and observational parameters are given in Table 1.

Digital correlators were configured for a 320 MHz band-

<sup>1</sup> Present address: National Radio Astronomy Observatory, 949 North Cherry Avenue, Tucson, AZ 85721-0655.

<sup>2</sup> Present address: Institute of Astronomy and Astrophysics, Academia Sinica, Taipei, Taiwan 115.

TABLE 1  
PARAMETERS FOR W51 OBSERVATIONS

Parameter	1995 December 14, 15	1996 January 21, 22	1996 February 22, 23
Array configuration .....	D	AB	C
Flux calibrator .....	Uranus	NRAO 530	Uranus
Phase calibrator .....	1749+096	1749+096	1749+096
	2149+096	2149+096	2149+096
Bandpass calibrator .....	3C 273	NRAO 530	3C 273
Bandwidth (MHz) .....	320	320	320
Spectral resolution .....	312.5 kHz (0.6 km s <sup>-1</sup> )	312.5 kHz	312.5 kHz
Primary beam (arcsec) .....	45	45	45
Baseline (m) .....	10–81	17–365	12–165

width with 1024 channels, yielding an equivalent resolution of 0.6 km s<sup>-1</sup> at 147 GHz. Broadband gain and phase calibrations were carried out every 10–15 minutes with respect to quasars 1749+026 or 2149+096. The gain and phase variations across the intermediate frequency band were calibrated with 3C 273 or NRAO 530. Uranus and NRAO 530 were observed to establish the absolute flux levels, which are accurate to about 20%.

Visibilities were calibrated with the NMA UVPROC2 software package. Imaging and self-calibration were performed in MIRIAD. The 2 mm continuum is constructed from a 25 km s<sup>-1</sup> wide window of line-free channels.

The noise levels of the naturally weighted maps are 0.04 Jy beam<sup>-1</sup> for the continuum and 0.25 Jy beam<sup>-1</sup> per 0.6 km s<sup>-1</sup> channel. The rms in the uniform-weighted maps is normally 50% higher.

### 3. RESULTS

#### 3.1. Line Spectra in the 320 MHz Window

Besides the CS (3–2), CH<sub>3</sub>CN (8–7), and H35 $\alpha$ , a number of other spectral lines were detected within the 320 MHz band. Figure 1 shows the spectra from the position of the

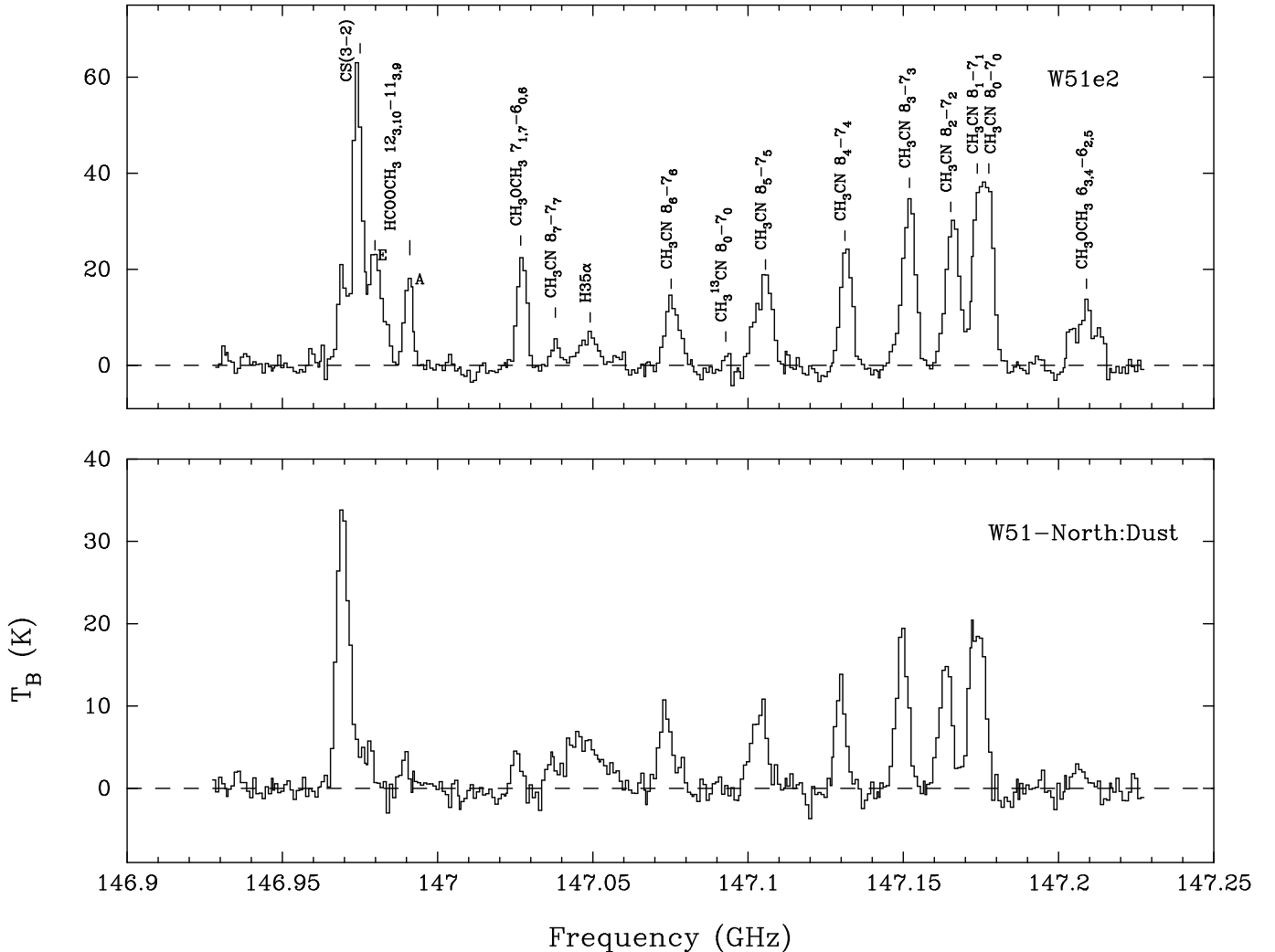


FIG. 1.—Line spectra from the position of W51e2 and W51-North:dust. Line frequencies correspond to the rest frequency when  $V_{\text{LSR}} = 60 \text{ km s}^{-1}$ .

W51e2 H II region and the W51-North:dust continuum peak.

The identification of the lines was based on frequencies and line strengths listed in the Lovas (Lovas 1992) and the Jet Propulsion Laboratory catalogs and the observations of the Orion region by Loren & Mundy (1984). The CS line is blended with spectra from other molecules. The two peaks 8.6 and 19 MHz blueshifted from the CS line are the  $\text{HCOOCH}_3$  ( $12_{3,10}$ – $11_{3,9}$ ) *E* and *A* components. The third peak 3 MHz redshifted from the CS line is likely part of the CS spectrum, since it disappears toward the W51-North region.

### 3.2. Distribution of Gas and Dust

#### 3.2.1. Continuum

Figure 2 shows the 2 mm continuum emission toward the W51e1/W51e2 region and W51-North. Also shown in the figure is the integrated line emission of the CS (3–2),  $\text{CH}_3\text{CN}$  (8–7), the radio recombination line (RRL) H35 $\alpha$ ,  $\text{CH}_3\text{OCH}_3$  ( $7_{1,7}$ – $6_{0,6}$ ) and ( $6_{3,4}$ – $6_{2,5}$ ), and  $\text{HCOOCH}_3$  ( $12_{3,10}$ – $11_{3,9}$ ) lines. In all cases, channels with detectable signals have been integrated.

In the W51e1/W51e2 region, the 2 mm continuum emission is found to be associated with UC H II regions. The one to the north coincides with the H II region e2. This source, which is resolved with a  $1''.3$  beam, consists of a compact structure of  $2''.8 \times 2''.0$  at a position angle of  $-65^\circ$  embedded in a more extended envelope. The peak of the emission is  $1.0 \text{ Jy beam}^{-1}$ , and the integrated flux of the source is 3.7 Jy. Extrapolating the optically thin centimeter free-free emission from the H II region to 2 mm assuming  $F_\nu \propto \nu^{-0.1}$ , we find that the contribution of the free-free emission is about 0.4 Jy. Hence, the dust emission dominates the 2 mm continuum (see also § 4.5.2).

The northwest-southeast extension of dust continuum near e2 resembles the distribution of  $\text{NH}_3$  at similar angular resolution (Zhang & Ho 1997). In particular, the extension  $2''$  southeast of e2 coincides with the warm  $\text{NH}_3$  marked by its (3, 3) emission, suggesting that this extended emission arises from the hot dust in the cloud core.

The 2 mm continuum emission toward the south of the e1/e2 region coincides with the UC H II regions e1 and e8. Separated by only  $2''$ , e1 and e8 are barely resolved in the 2 mm continuum map. We note that there is no 2 mm continuum emission detected toward e3 and e4 at the achieved sensitivity level ( $1 \sigma = 0.04 \text{ Jy per } 1''.3 \text{ beam}$ ), although both sources are clearly detected at 3.6 cm with 6 and 4 mJy, respectively (Gaume et al. 1993).

The integrated flux of the southern continuum source in the e1/e2 region is about 2 Jy. It is difficult to assign flux to the individual H II regions e1 and e8. Nevertheless, the e8 component, which is 3 times fainter than e1 (0.08 Jy) at 1.3 cm, seems to be stronger than e1 at 2 mm. Subtracting the free-free emission, we estimate the 2 mm dust emission to be 1–2 Jy for e8 and less than 1 Jy for e1.

The 2 mm continuum emission toward W51-North is extended. However, it does not have the same distribution as the 1.3 cm continuum. In particular, there is a relatively compact 2 mm continuum peak, which we designated as W51-North:dust, at  $\alpha(1950) = 19^{\text{h}}21^{\text{m}}22^{\text{s}}.3$  and  $\delta(1950) = 14^\circ25'12''.8$ . This source, which lies to the southeast of IRS 2, is outside the projected boundary of the 1.3 cm continuum. The flux of the peak is about  $2 \text{ Jy beam}^{-1}$ . Compared with the nondetection at the centimeter wavelength, the 2 mm

continuum emission is almost entirely from the dust.

The spectral energy distribution of the H II regions is not well constrained at shorter wavelengths, especially for e1 and e8, owing to source confusion. We assume optically thin dust emission to estimate the mass in dust. The dust opacity is assumed to vary as  $\nu^\beta$  with  $\beta = 1$ . For a dust temperature of 100 K (based on the temperature determined from  $\text{CH}_3\text{CN}$ , see § 3.4) and gas-to-dust ratio of 100, we obtain gas mass of  $8 \times 10^2 M_\odot$ ,  $(2\text{--}4) \times 10^2 M_\odot$ , less than  $2 \times 10^2 M_\odot$ , and  $4 \times 10^2 M_\odot$  in the e2, e8, e1, and W51-North: dust cores, respectively.

#### 3.2.2. CS Emission

In the W51e1/W51e2 region, two strong condensations of the CS (3–2) emission are found in the integrated map. They are both in the vicinity of the 2 mm continuum peaks and are coincident with the  $\text{NH}_3$  cores. In the integrated line map, these two cores are slightly offset from the continuum sources e2 and e8 (Fig. 2). This is partially caused by absorption against the continuum source, which reduces the line intensity toward the H II regions e2 and e8. Figure 3 shows the channel maps of the CS emission. To guide core identification, we marked the positions of the continuum sources e1, e2, and e8 in the region. The cloud systemic velocities of the e2 and the e8 cores are  $55 \text{ km s}^{-1}$  and  $59 \text{ km s}^{-1}$ , respectively (see § 3.3.1). The emission at less than  $45 \text{ km s}^{-1}$  is contaminated by the emission from the  $\text{HCOOCH}_3$  line. In the blueshifted and redshifted velocity channels ( $45\text{--}52$  and  $61\text{--}65 \text{ km s}^{-1}$ ), the CS emission is closely associated with the e2 and e8 continuum sources. In the intermediate velocities, the CS is extended with pronounced negative sidelobes due to poor  $u$ ,  $v$  coverage and lack of short spacing visibilities. Nevertheless, even for the intermediate velocities, the core structure is obvious except near the emission dips around  $57 \text{ km s}^{-1}$  for e2.

Besides the two strong condensations identified in the integrated emission, two additional clumps are apparent in the channel maps of CS in Figure 3a. One clump lies  $9''$  south of e8 (see the channel map of  $51 \text{ km s}^{-1}$  in Fig. 3a) and coincides with an  $\text{NH}_3$  core (see Ho & Young 1996) and an  $\text{H}_2\text{O}$  maser. The other clump, about  $6''$  west of e8 (see the channel map of  $58 \text{ km s}^{-1}$  in Fig. 3a), has a peak velocity of  $58 \text{ km s}^{-1}$  and extended blueshifted wing up to  $45 \text{ km s}^{-1}$ . The mass in the condensation, though difficult to estimate because of high opacity in CS emission, is no doubt much smaller than in the e2 and e8 cores based on the integrated intensity map (Fig. 2a). This core, which is not apparent in  $\text{NH}_3$ , is also seen in  $\text{HCO}^+$  (Rudolph et al. 1990). A  $\text{NH}_3$  maser (Zhang & Ho 1997) was found to lie about  $4''$  south of the CS condensation and shows blueshifted emission. This blueshifted emission in the CS and  $\text{NH}_3$  lines may trace a molecular outflow. It is possible that both CS condensations mark the site of star formation.

The CS emission in W51-North displays an east-west extension (Figs. 2 and 3), similar to the  $\text{NH}_3$  gas. The dense gas is centered near the W51-North:dust and the known UC H II d2 (Gaume et al. 1993) sources. The CS emission extends to the west beyond the position of the  $\text{NH}_3$  (3, 3) maser (Zhang & Ho 1995)  $8''$  west of d2. There is a narrow CS component  $10''$  east of d2, centered at  $59 \text{ km s}^{-1}$  (see Fig. 3). The line width is about  $3.7 \pm 0.5 \text{ km s}^{-1}$ , which is significantly narrower than the line width near d2. There are no corresponding continuum sources detected in the radio or infrared wavelengths.

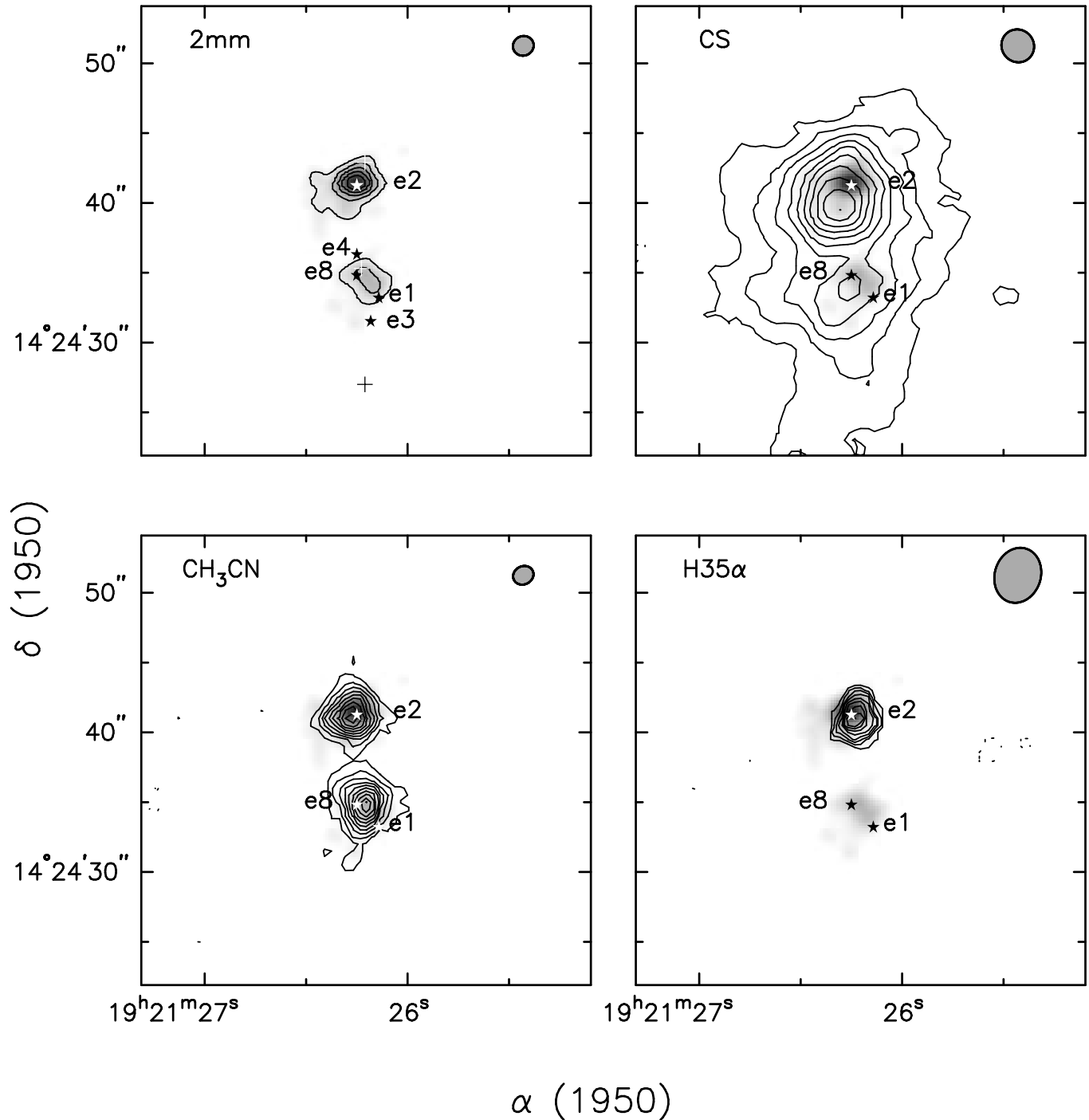


FIG. 2a

FIG. 2.—The 2 mm continuum and the line emission of the CS (3–2),  $\text{CH}_3\text{CN}$  (8–7),  $\text{H35}\alpha$ ,  $\text{CH}_3\text{OCH}_3$  (12–11), and  $\text{HCOOCH}_3$  (7–6) and (6–6) integrated over the whole range of line emission. The synthesized beams for contour maps are plotted at the upper right-hand corner of each panel. The stars mark the position of the known centimeter continuum sources, and the crosses denote the  $\text{H}_2\text{O}$  masers (Genzel et al. 1982). The dust continuum source W51-North:dust is marked with triangles. (a) The e1/e2 region in continuum and in CS,  $\text{CH}_3\text{CN}$ , and  $\text{H35}\alpha$ . The gray scales are the 2 mm continuum emission plotted linearly from 0.01 to  $1.4 \text{ Jy beam}^{-1}$ . The contours for the continuum are plotted at  $-0.2, 0.2, 0.4, 0.6, 0.8, 1.0, 1.5$ , and  $2.0 \text{ Jy beam}^{-1}$ . The contours for the integrated line emission are plotted at every 10% of the peaks, which are 80 (for CS), 55 (for  $\text{CH}_3\text{CN}$ ), and  $6.3$  (for  $\text{H35}\alpha$ )  $\text{Jy beam}^{-1} \text{ km s}^{-1}$ . (b) Same as (a), but for W51-North. (c) Integrated line emission of  $\text{CH}_3\text{OCH}_3$  (7–6) and (6–6) and  $\text{HCOOCH}_3$  (12–11) toward the e1/e2 region and W51-North. The contours are drawn at  $-4.5, -3, -1.5, 1.5, 3, 4.5, 6, 13.5, 22.5$ , and  $30 \text{ Jy beam}^{-1} \text{ km s}^{-1}$ .

### 3.2.3. $\text{CH}_3\text{CN}$

In the W51e1/W51e2 region, the  $\text{CH}_3\text{CN}$  (8–7) emission is compact and coincides well with the locations of the UC H II regions (see Figs. 2 and 4). One peak of  $\text{CH}_3\text{CN}$  core coincides with the position of e2, while the centroid of the e8 core lies within  $0''.4$  of the corresponding continuum source.

The e2 core is resolved with the  $1''.3$  beam, yielding a size of  $2''.4$ . The e8 core is slightly elongated with a size of  $2''.9 \times 2''.1$  and a position angle of  $13^\circ$  for the major axis. The core in W51-North shows an east-west extension similar to that of CS and  $\text{NH}_3$  but with a much smaller spatial extent. This core is well centered on the W51-North:dust source, with some extra  $\text{CH}_3\text{CN}$  emission to the southeast and west of

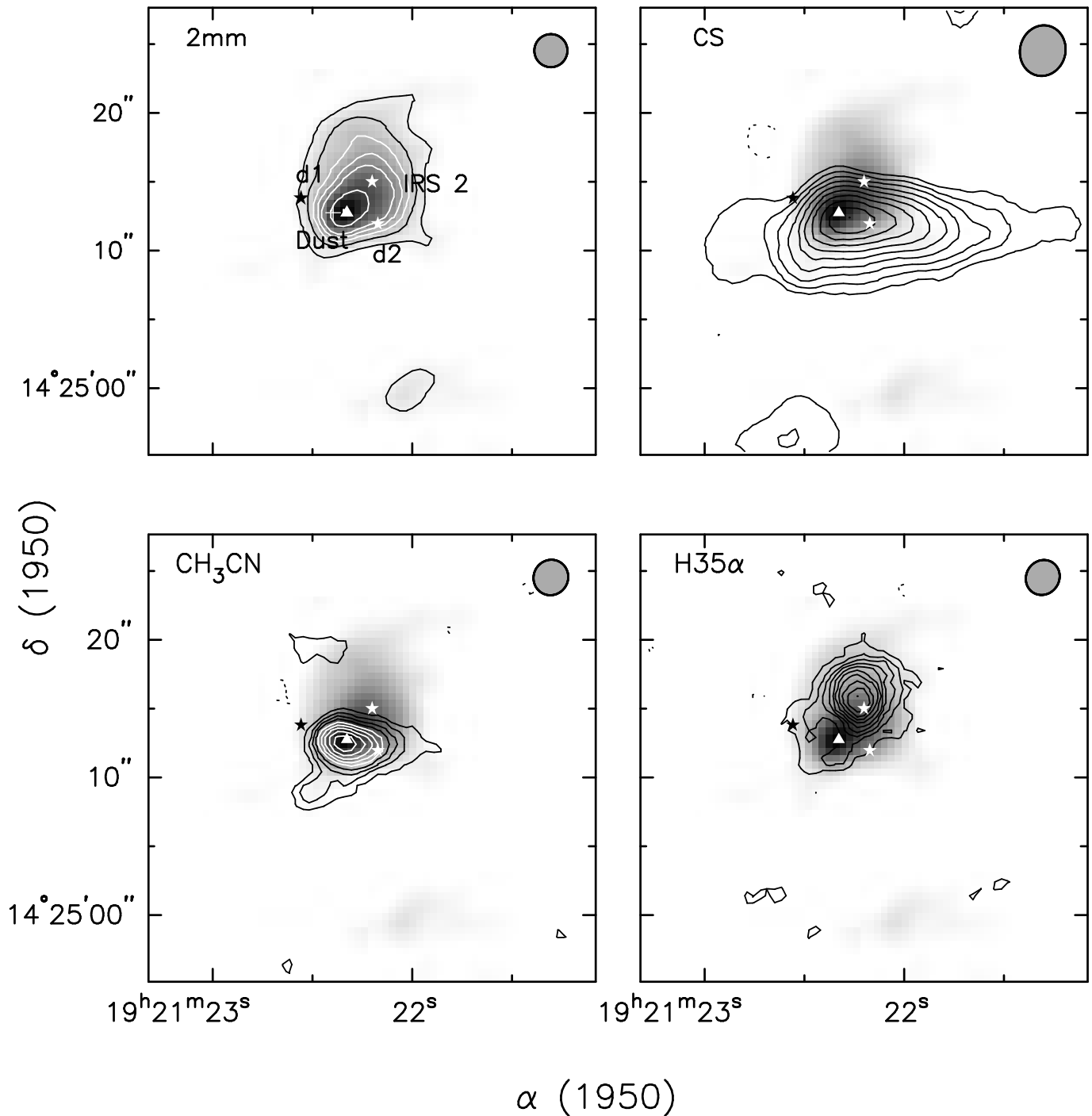


FIG. 2b

the core. There are hints of this extension to the southeast in CS and H35 $\alpha$ .

The integrated CH<sub>3</sub>CN emissions of the different  $K$  components in Figure 4 show that the emission in the lower  $K$  components is more extended. This indicates temperature variations in the CH<sub>3</sub>CN cores. Since the lower  $K$  components have larger optical depths (see § 3.4 and Appendix B) and lower excitation temperatures, they trace the cooler part of the CH<sub>3</sub>CN cores.

#### 3.2.4. Radio Recombination Line

Ultraviolet radiation from newborn massive stars ionizes

the gas in the surroundings, which in turn produces hydrogen recombination lines. Since the thermal free-free emission from most H II regions is optically thin at 2 mm except for some rare instances (Martín-Pintado et al. 1989), recombination lines will escape without attenuation. In the e1/e2 region, weak H35 $\alpha$  emission is detected toward the e2 component with a FWHM = 13.5 km s<sup>-1</sup>. This is perhaps the narrowest hydrogen recombination line measured so far in a fully ionized UCH II region.

The H35 $\alpha$  emission is also detected in W51-North, centered to the northwest of the dust peak and coincident with the centimeter continuum emission. The line widths here

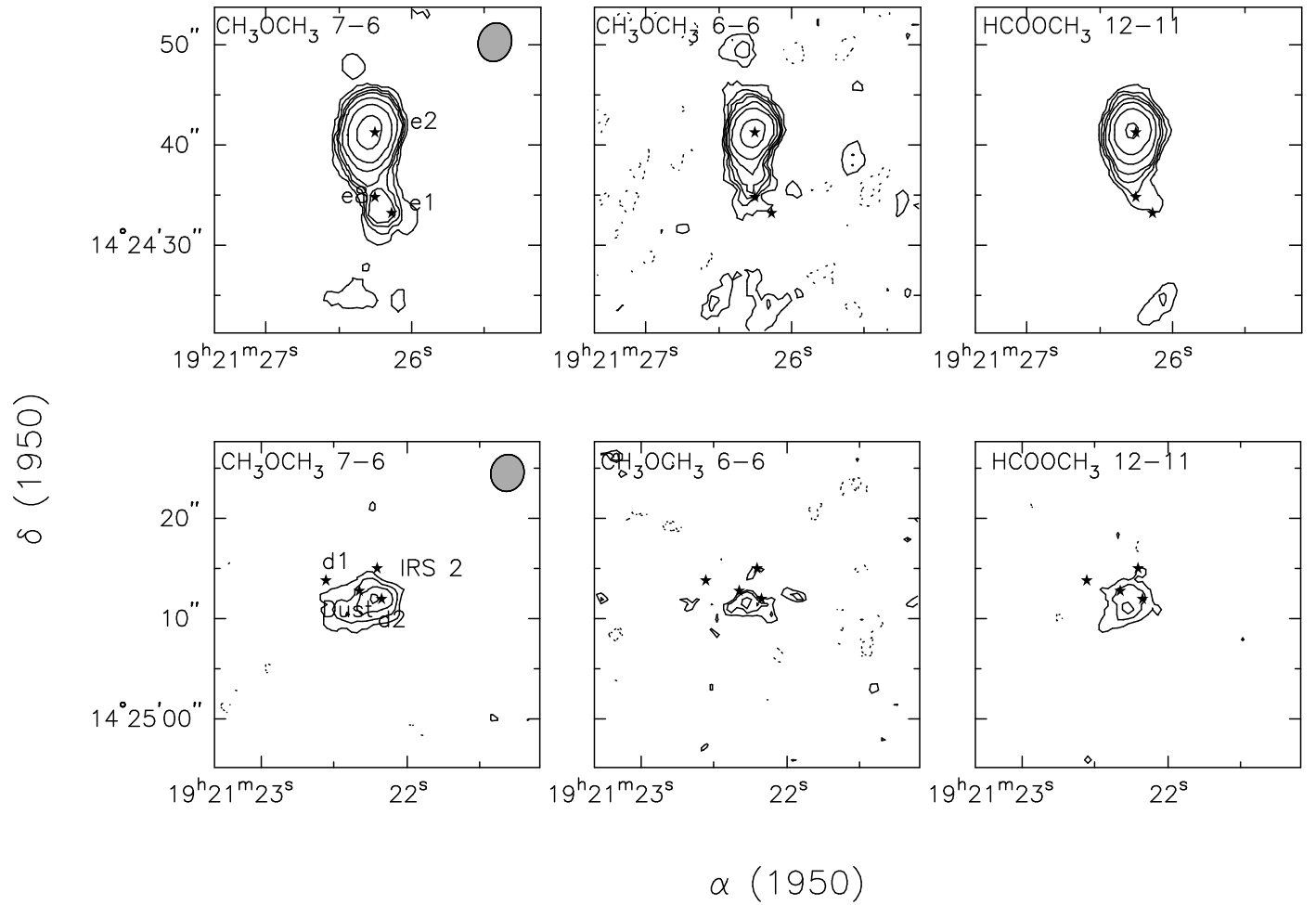


FIG. 2c

are broader, greater than  $25 \text{ km s}^{-1}$  FWHM (see Fig. 5). The weak H35 $\alpha$  emission at the position of the W51-North: dust is consistent with the idea that the central source, which is forming a massive star or stars, has not yet produced significant ionization.

Contrary to the 2 mm observations, the measurement of H92 $\alpha$  at 3.6 cm (Mehringer 1994) produced a detection of 10 mJy beam $^{-1}$  toward e1 and nondetection toward e2, e8, and W51-North:dust at a sensitivity of less than 0.5 mJy. The nondetection of the RRL from e2 at 3.6 cm is most likely due to the optically thick H II region, which attenuates the line emission. On the other hand, the null result of the 2 mm RRL toward e1 is due to the lower sensitivity of this experiment.

### 3.2.5. Oxygen-bearing Molecules

Line emission of oxygen-rich molecules  $\text{CH}_3\text{OCH}_3$  and  $\text{HCOOCH}_3$  is detected toward the UC H II regions. The strongest emission is found toward e2 (see Fig. 2). It is shifted less than  $1''$  to the east of the continuum source. In contrast to  $\text{CH}_3\text{CN}$  and CS, the  $\text{CH}_3\text{OCH}_3$  emission at e1 appears to be as strong as that from the e8 core.

In W51-North, the emission of the  $\text{CH}_3\text{OCH}_3$  and  $\text{HCOOCH}_3$  lines is mainly concentrated around d2 and W51-North:dust. The extension of the emission to the southeast of d2 coincides with the emission seen in  $\text{CH}_3\text{CN}$  and CS.

## 3.3. Kinematics

### 3.3.1. Infall in W51e2 and W51e8 Cores

As discussed in Appendix A, for a centrally condensed core under collapse, one expects line asymmetry in optically thick transitions with respect to the core systemic velocity. In the presence of inward motions, the blue part and the red part of the line arise from the rear and the front side of the cloud, respectively. The red part of the emission of  $\tau \sim 1$  comes primarily from the outer and cooler region in the front side. On the other hand, the blue part of the emission of  $\tau \sim 1$  comes from the inner, and thus hotter, region in the rear side. This geometrical asymmetry for the emitting regions with respect to the core center gives rise to the stronger blue shoulder in line profiles relative to the red shoulder. The disparity between the blue and red shoulders decreases with the decrease of optical depth. The line becomes symmetric when it is optically thin because emission from different parts of the core along the line of sight escapes without trapping (see also Anglada et al. 1987; Zhou et al. 1990, 1993).

This pattern of infall asymmetry exists among the line profiles from the e2 and e8 cores. Figure 6 shows spectra of the CS (3–2),  $\text{CH}_3\text{CN}$  (8–7),  $\text{CH}_3\text{OCH}_3$  (7–6), and  $\text{HCOOCH}_3$  (12–11) lines at the position of the H II regions

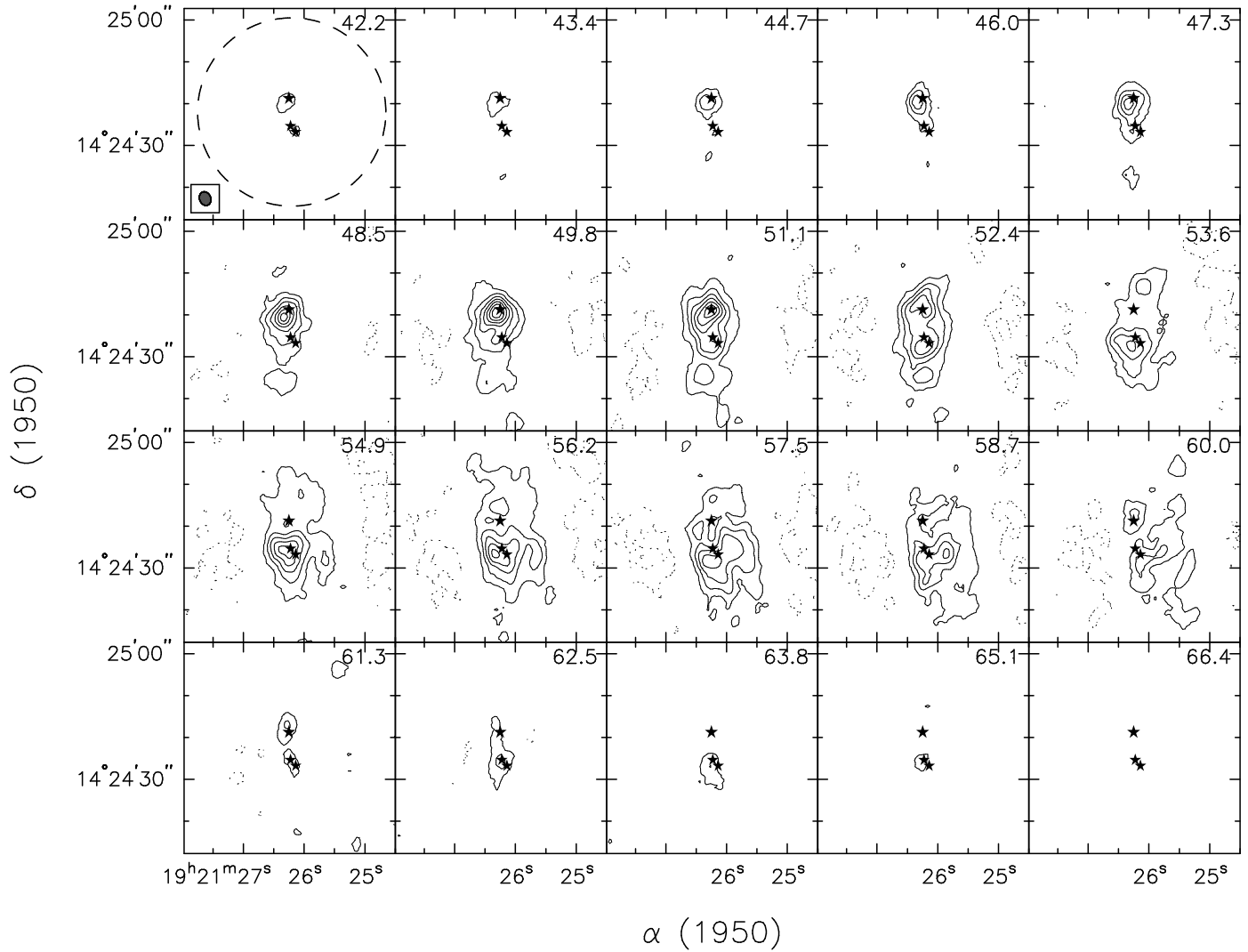


FIG. 3a

FIG. 3.—Channel maps of the CS (3–2) for (a) the e1/e2 region and (b) W51-North. The maps are plotted every other channel with contour levels starting from  $\pm 1.2 \text{ Jy beam}^{-1}$  and separated by  $\pm 1.2 \text{ Jy beam}^{-1}$ . The dotted lines denote negative emission. The stars are the continuum sources labeled in Fig. 2. In (a), only e1, e2, and e8 are labeled. The synthesized and the primary (dashed line) beams are indicated in the first panel. The velocity (in  $\text{km s}^{-1}$ ) of the channel is indicated in the upper right-hand corner of each panel.

e2 and e8. The lines of the oxygen-bearing molecules toward e8 are too faint and are omitted in Figure 6b. For both cores, the optical depths of the  $K = 0$  component of the  $\text{CH}_3\text{CN}$  (8–7) derived from the  $\text{CH}_3\text{CN}$  to  $\text{CH}_3^{13}\text{CN}$  line ratio are about 2. If the  $A$  and  $E$  species have equal abundances, the opacity ranks in a decreasing order as  $K = 0, 1, 3, 2, 4, 5$ , and 6 for conditions in the W51 dense cores (see § 3.4 and Appendix B). The more optically thick  $K = 0$  and 1 components of  $\text{CH}_3\text{CN}$  are not included in Figure 6 because they are blended together. The  $K > 4$  lines are omitted in the figure because the hyperfine splittings are larger than the spectral resolution of the data, and the kinematics are therefore confused.

The simultaneous least-squares fit of Gaussian profiles on all the  $K$  components of the  $\text{CH}_3\text{CN}$  (8–7) line yields a cloud systemic velocity of 55 and 59  $\text{km s}^{-1}$  for the e2 and the e8 cores, respectively. Toward both e2 and e8, it appears that the  $K = 2, 3$ , and 4 lines of the  $\text{CH}_3\text{CN}$  (8–7) transition

are asymmetric with respect to the systemic velocity, with the blue side of the profile stronger than the red side. This asymmetry increases toward the more optically thick lines. The CS (3–2) line, which is likely the most optically thick transition among all the lines, is heavily skewed toward the blue, with the red side greatly suppressed toward both e2 and e8. The spectral lines of the oxygen-bearing molecules toward e2 also show some degree of asymmetry, although the optical depth is not determined.

As seen in Figure 6, both the CS and the  $\text{CH}_3\text{CN}$   $K = 3$  spectra from e2 and e8 show infall asymmetry. However, this asymmetry is only confined to a few arcseconds around the H II region. Figure 7 presents the CS (3–2) and  $\text{CH}_3\text{CN}$  (8<sub>3</sub>–7<sub>3</sub>) spectra at e2 and the positions off e2. The CS (3–2) and  $\text{CH}_3\text{CN}$  (8<sub>3</sub>–7<sub>3</sub>) lines display symmetric profiles at positions a few arcseconds away from e2. The central velocity coincides with the cloud systemic velocity. We interpret this in terms of the optical depth effect and localized infall.

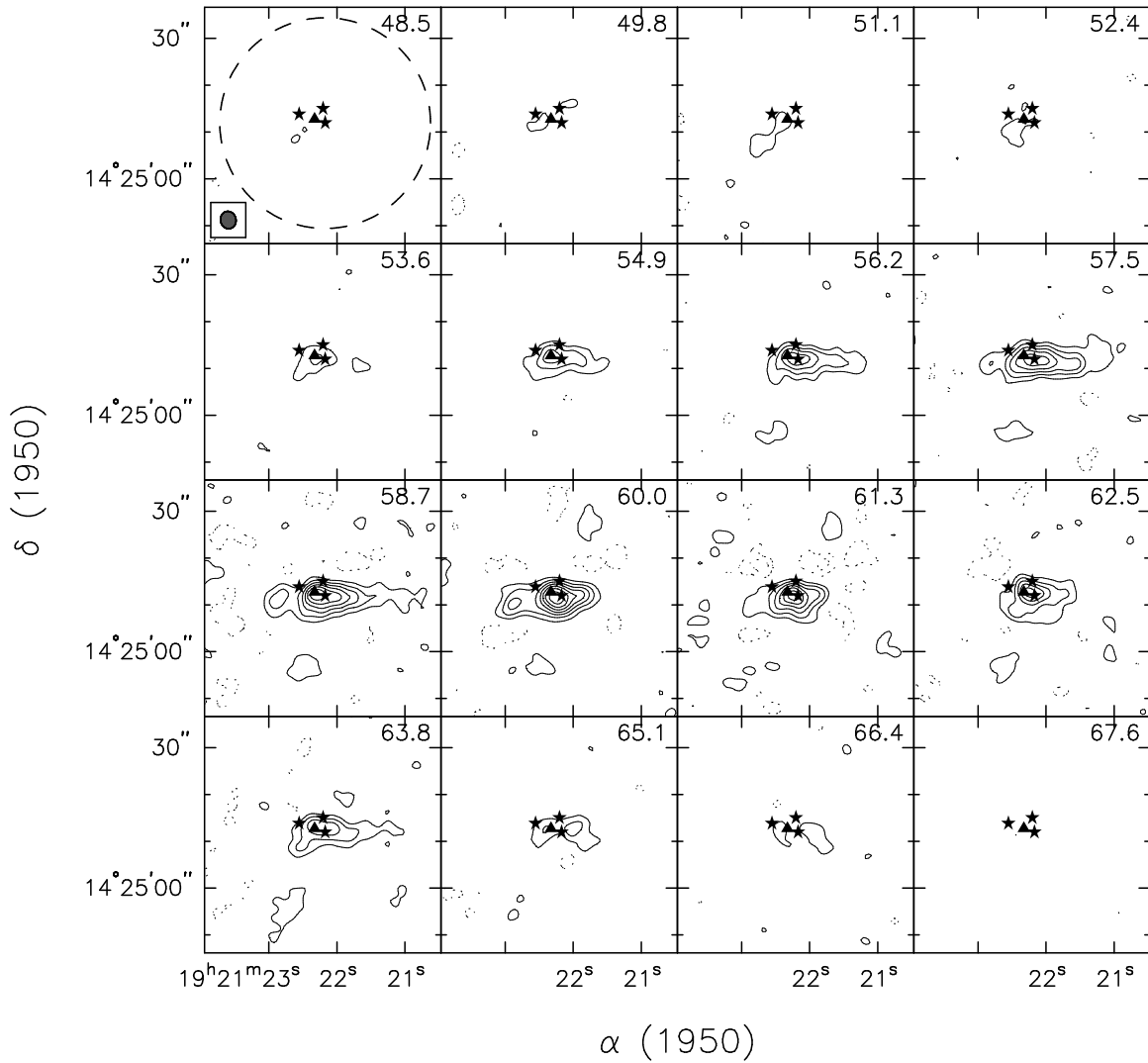


FIG. 3b

Because of the decrease in path length and densities, one expects that the optical depths at the off positions are smaller than those near the core center. In a spherical cloud, a line profile becomes symmetric when it is optically thin regardless of the presence of infall. On the other hand, a line also becomes symmetric in the absence of infall regardless of the values of optical depths. The change of symmetry seen in Figure 7 is consistent with a localized, radial infall in a spherical cloud.

The presence of a compact continuum source at the center of the cloud core enhances the asymmetry of line profiles. This provides additional constraints on the locations of the emitting gas with respect to the source (see Appendix A for detailed discussions). The enhancement depends on the contrast of the brightness temperature of the continuum and the excitation of the lines. Because the continuum emission, particularly that from H II regions, is often more centrally condensed than line emission, the brightness temperature of the continuum should rise faster than the line emission when the source is observed with finer angular resolutions. As a result, line asymmetries become more prominent. If the continuum temperature

exceeds the line temperature, the redshifted profile turns into absorption (see Zhang & Ho 1997). Such absorption features cannot be seen in Figure 6 because the continuum temperature does not exceed the line excitation temperature.

We note that this method does not rely on assumptions of excitation as described at the beginning of this section. It provides an independent test to the infall interpretation. As an application to W51, we imaged the CS emission at different angular resolutions. We choose the CS line because of its high line intensity and large optical depth.

Figure 8 presents the CS line toward e2 and e8 at different angular resolutions, which are derived from the natural or robust weightings of the  $u, v$  visibilities from the different array configurations. Note that the CS (3–2) line from e2 is blended with the  $\text{HCOOCH}_3$  ( $12_{3,10}$ – $11_{3,9}$ )  $A$  and  $E$  lines, which appear at 15 and 37  $\text{km s}^{-1}$ , respectively. In spite of this confusion, the blueshifted portions of the CS line from both e2 and e8 appear to be similar at different angular resolutions. The redshifted emission (around 57  $\text{km s}^{-1}$  for e2 or 62  $\text{km s}^{-1}$  for e8) is suppressed at all angular resolutions. In particular, this dip is enhanced at smaller



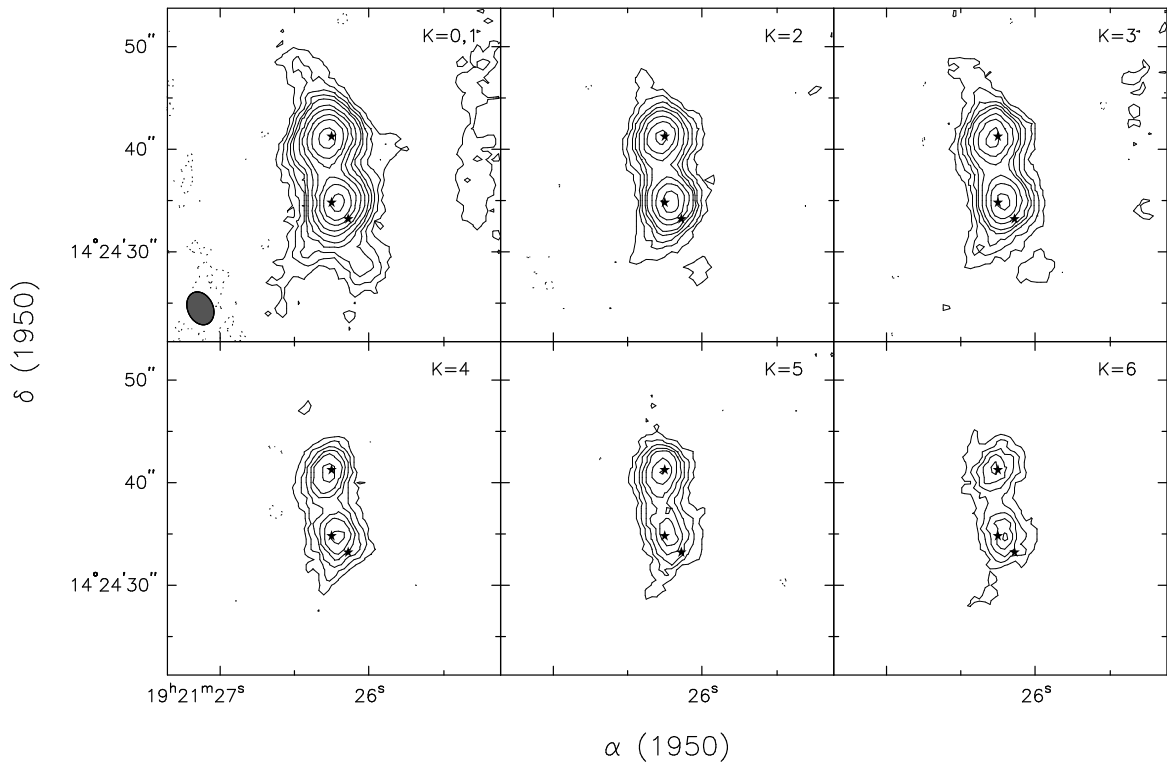


FIG. 4a

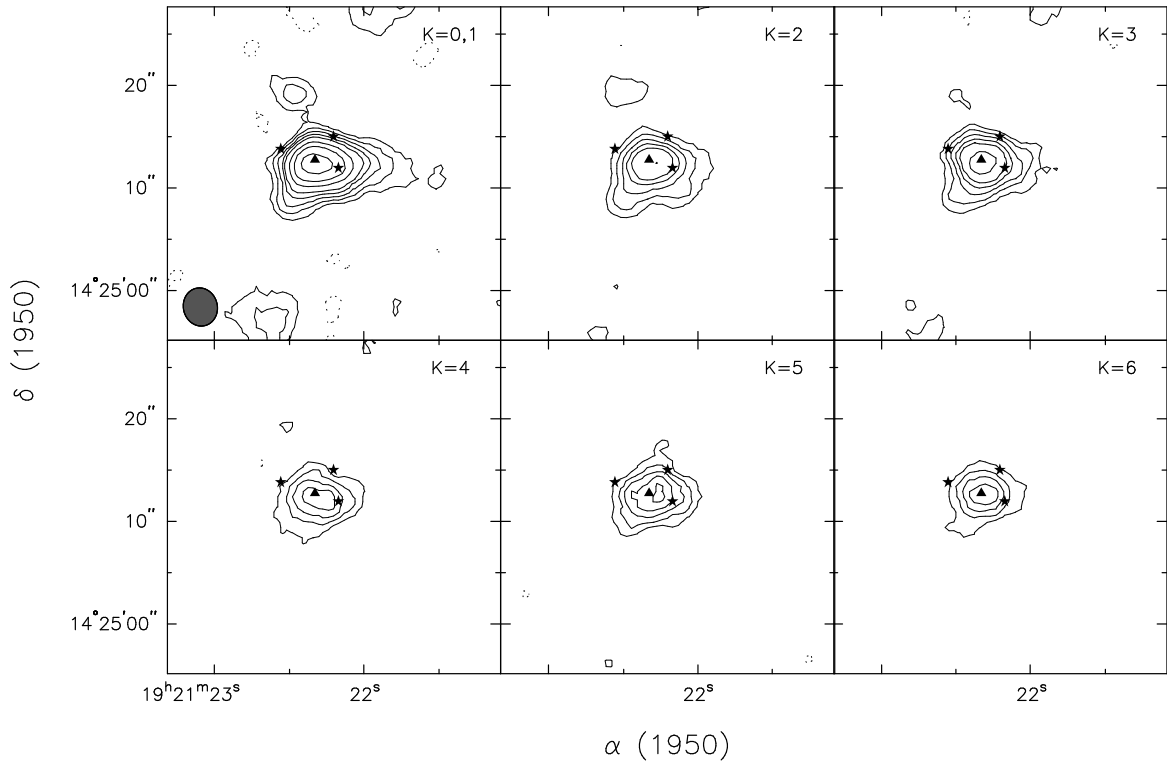


FIG. 4b

FIG. 4.—Integrated emission of different  $K$  components of the  $\text{CH}_3\text{CN}$  (8–7) for (a) the e1/e2 region and (b) W51-North. The contour levels are plotted at  $\pm 2.5, \pm 5, \pm 7.5, \pm 10, \pm 12.5, 17.5, 22.5, 30, 37.5$ , and  $50 \text{ Jy beam}^{-1} \text{ km s}^{-1}$ . The dotted lines denote negative emission. The stars are the continuum sources labeled in Fig. 2. In (a), only e1, e2, and e8 are labeled. The beam size and the  $K$  components are indicated in the lower left-hand and upper right-hand corners of the panel, respectively.

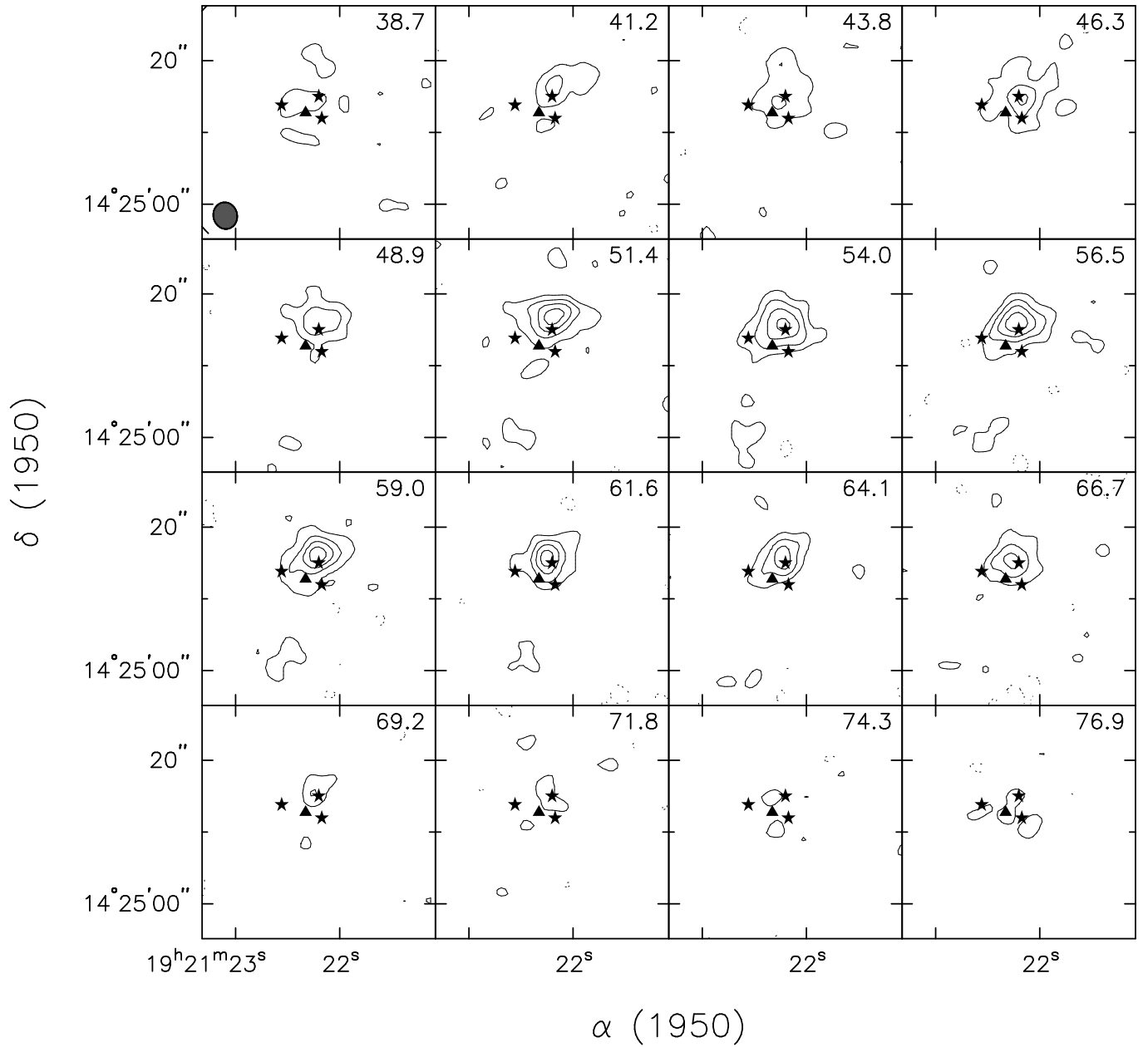


FIG. 5.—Contour maps of H35 $\alpha$  toward W51-North. The data are averaged to  $1.3 \text{ km s}^{-1}$  and are plotted every other channel at contour levels starting at  $\pm 0.6 \text{ Jy beam}^{-1}$  separated by  $\pm 0.6 \text{ Jy beam}^{-1}$ . The dotted lines denote negative emission. The stars are the continuum sources labeled in Fig. 2. The beam size ( $3''.7 \times 3''.3$  at P.A. =  $-13^\circ$ ) and the velocity (in  $\text{km s}^{-1}$ ) of the channel are indicated in the lower left-hand and upper right-hand corners of the panel, respectively. The channel maps of H35 $\alpha$  toward the e1/e2 region are not presented owing to their weak signals.

synthesized beams and appears in absorption toward e2 at about  $1''$  resolution. The velocities of the blueshifted emission and the redshifted absorption are consistent with those in NH $_3$  (Ho & Young 1996; Zhang & Ho 1997). There is another absorption feature toward e2 in the CS spectrum at  $68 \text{ km s}^{-1}$ . This feature is also seen toward W51-North as well as in HCO $^+$  (Rudolph et al. 1990). This absorption has been attributed to foreground clouds that are not associated with e2 and e8 (Ho & Young 1996).

These pieces of evidence, i.e., asymmetric profiles in optically thick transitions and the increase of asymmetry with the increase of optical depths and angular resolutions, strongly indicate that the blueshifted emission arises behind the continuum source, and the redshifted absorbing gas is in

the front. This geometrical arrangement establishes inward motions toward the star.

Figure 9 presents the position-velocity plot of the CS (3–2) across the e2 core in comparison with the NH $_3$  (2, 2) from Zhang & Ho (1997) (Fig. 10 [Pl. 26]). The suppressed CS emission near [position, velocity] =  $[0'', 57 \text{ km s}^{-1}]$  is in good agreement with the NH $_3$  absorption. The emission in CS between 48 to  $56 \text{ km s}^{-1}$  forms a C-shaped structure around the absorption dip at e2, similar to that in NH $_3$ . The radius of the C is about  $3''$ . This C feature in CS indicates a radial pattern for the infalling gas, consistent with the velocity structures identified in NH $_3$  (Ho & Young 1996; Zhang & Ho 1997).

Signatures of infall were also searched for toward W51-

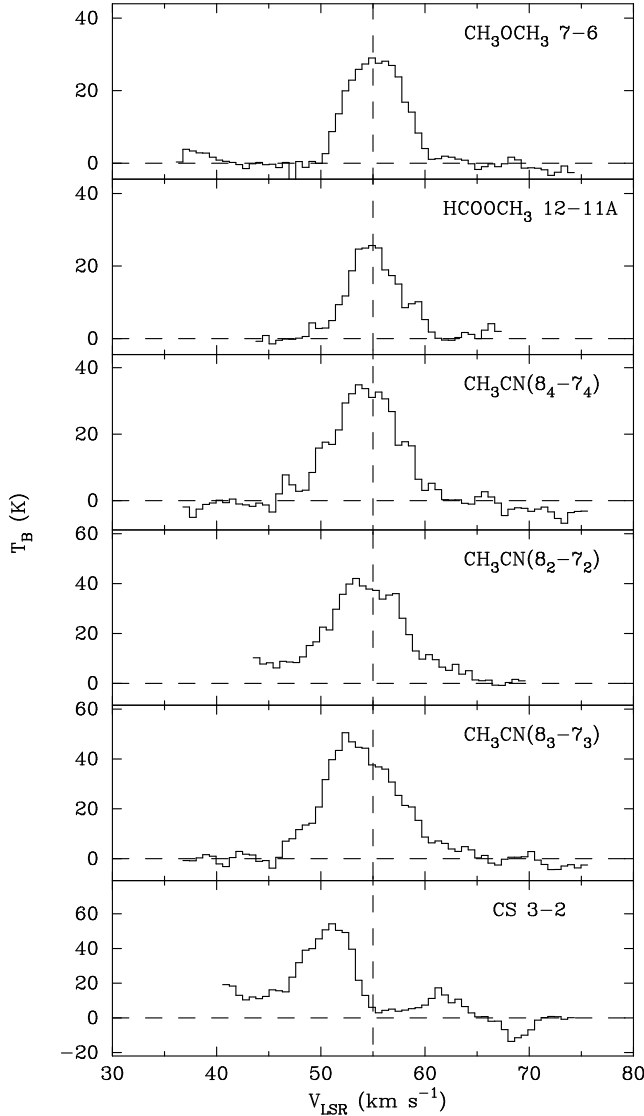


FIG. 6a

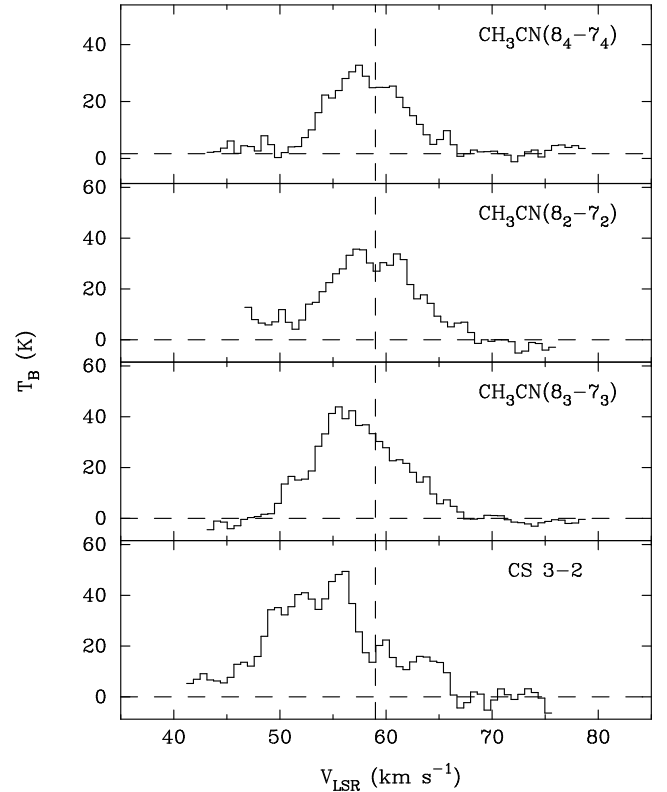


FIG. 6b

FIG. 6.—Spectral line profiles of the  $\text{CH}_3\text{OCH}_3$  (7–6),  $\text{HCOOCH}_3$  (12–11),  $\text{CH}_3\text{CN } J_K - J_{K'} = (8_K - 7_K)$ , and the CS (3–2) at the position of (a) W51e2 and (b) e8. All the spectra are made with a  $2''.5$  beam. The vertical dashed line marks the core systemic velocity.

North:dust and d2. There are no consistent patterns among the spectral lines. This is likely due to cloud confusion, since W51-North:dust is only  $2''.3$  southeast of d2. They are not spatially resolved at greater than  $2''$  resolution.

### 3.3.2. Rotation in the e2 and e8 Cores

The strong and compact  $\text{CH}_3\text{CN } (8_3 - 7_3)$  emission allows us to examine the velocity gradient across the core. Since the  $\text{CH}_3\text{CN}$  emission toward e2 and e8 has a simple morphology (see Fig. 2a), we determine the emission peak of each velocity channel through elliptical Gaussian fitting. Figure 11 shows the centroid position of each channel versus the velocity of the channel.

The error bar plotted in Figure 11 represents the  $1\sigma$  uncertainty in the Gaussian fitting. The actual uncertainty in position can be significantly larger, depending upon the flux and the morphology of the emission. Typically, the astrometric uncertainty of an interferometric image due to thermal noise is about  $0.45[\theta/(S/N)]$  (Reid et al. 1988),

where  $\theta$  and  $S/N$  are the angular resolution and the signal-to-noise ratio of the image, respectively. For  $S/N = 10$ , we estimate the positional uncertainty to be  $\sim 0''.15$ .

The morphology of the  $\text{CH}_3\text{CN}$  emission also affects the accuracy of the fitted position. Since we assume a priori that the emission is elliptical, discrepancies in the shape will introduce errors to the position determination. With these error sources included, the uncertainty in position is perhaps  $0''.5$ .

In the e2 and e8 cores, it appears that the molecular gas is slightly offset from the continuum source as shown in  $\text{NH}_3$ , CS,  $\text{CH}_3\text{OCH}_3$ , and  $\text{HCOOCH}_3$ . The position and velocity are highly correlated (see the middle and the bottom panels of Fig. 11), indicating velocity gradients in both cores. In the e2 core, the gradient is mainly in the east-west direction. The least-squares fit to the data gives  $6.3 \pm 1.1 \text{ km s}^{-1}$  per  $1''$  in the east-west direction and  $-2.4 \pm 1.7 \text{ km s}^{-1}$  per  $1''$  in the north-south direction. A similar fit to the data in the e8 core gives a velocity gradient of  $2.5 \pm 2.8 \text{ km s}^{-1}$  per  $1''$

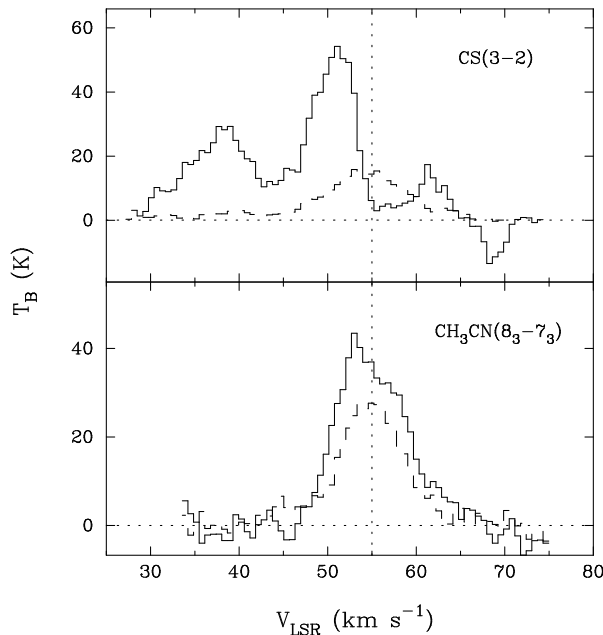


FIG. 7.—The CS (3–2) and  $\text{CH}_3\text{CN}$  ( $8_3-7_3$ ) lines from the position of W51e2 as compared with those from the positions off e2. The vertical, dotted line shows the cloud systemic velocity at  $55 \text{ km s}^{-1}$ . The dashed lines are the spectra from the off positions  $9''$  and  $3''$  north of e2 for the CS and  $\text{CH}_3\text{CN}$ , respectively.

in the east-west direction and  $-5.6 \pm 1.0 \text{ km s}^{-1}$  per  $1''$  in the north-south direction. We note that these gradients are averaged velocity shifts over scales greater than  $0.5''$ . The velocity structure within  $0.5''$  scales cannot be determined owing to positional uncertainties.

It is possible that these velocity gradients, which dominate in a particular direction, represent rotational motions in both cores. From the velocity gradient projected on right ascension and declination, one can determine the position angle of the rotational axis in the e2 and e8 cores, provided that the velocity gradient arises from rotational motions. We obtain  $\text{P.A.} = 20^\circ \pm 17^\circ$  for the e2 core and  $\text{P.A.} = 66^\circ \pm 27^\circ$  for the e8 core. The peak positions of the  $\text{CH}_3\text{CN}$  emission in Figure 11 are distributed in narrow strips orthogonal to the rotational axis. This flattening in the e2 and e8 cores, which is not apparent in the integrated emission, is consistent with the existence of rotation.

In the e2 core, the position angle of the projected rotational axis roughly agrees with that seen in  $\text{NH}_3$  at smaller than  $1''$  scales. Compared with the velocity shift at smaller than  $0.5''$  scales determined from  $\text{NH}_3$  (Zhang & Ho 1997), the  $6.3 \text{ km s}^{-1}$  gradient at  $1''$  scales indicates that the rotation is accelerated toward the inner part of the core. This result supports the suggestion in the paper by Zhang & Ho (1997) that the e2 core rotates and spins up during the course of collapse. The velocity gradient in the e8 core was not seen previously in  $\text{NH}_3$  owing to confusion from broad line widths.

### 3.3.3. Expanding Shell

Channel maps of the CS (3–2) line toward W51-North (see Fig. 3b) show that the east-west extension of the CS core varies with velocity. Starting from the  $53.6 \text{ km s}^{-1}$  channel, the CS emission west of d2 stretches further to the west in channels of higher velocities. The emission reaches the maximum extent to the west at the cloud velocity of about  $59 \text{ km s}^{-1}$ . Then, the emission recedes to the east toward more redshifted velocities. Starting from  $62 \text{ km s}^{-1}$ ,

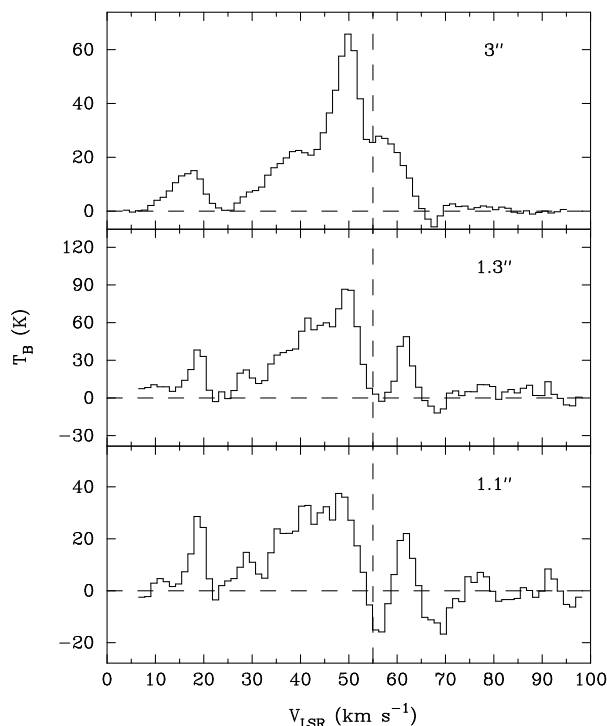


FIG. 8a

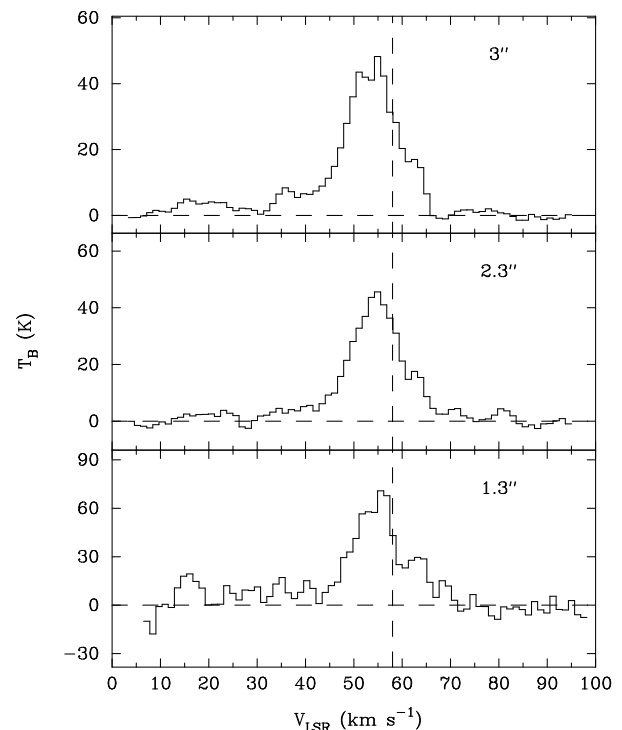


FIG. 8b

FIG. 8.—Spectral line profiles of the CS (3–2) at the position of (a) W51e2 and (b) e8 made from different angular resolutions. The vertical dashed line marks the core systemic velocity. The absorption feature near  $68 \text{ km s}^{-1}$  in (a) is likely due to foreground clouds.

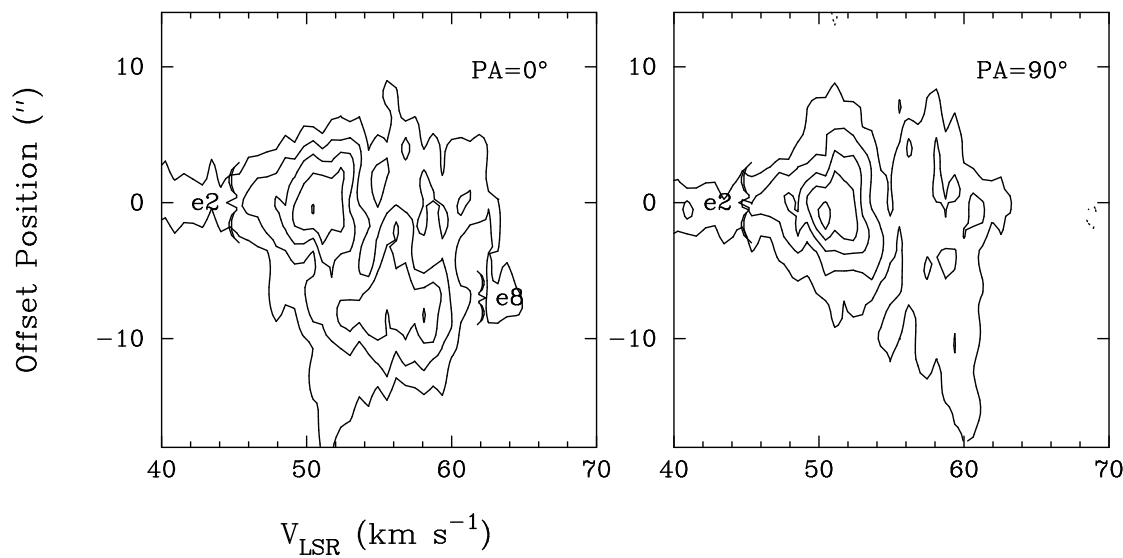


FIG. 9.—(a) Position-velocity diagram of the CS (3–2) line. The cut is offset from W51e2 at  $\alpha(1950) = 19^{\text{h}}21^{\text{m}}26^{\text{s}}.247$  and  $\delta(1950) = 14^{\circ}24'41''.3$  with position angles of  $0^{\circ}$  and  $90^{\circ}$ . The contours are plotted at  $1.2 \text{ Jy beam}^{-1}$  intervals starting from  $1.2 \text{ Jy beam}^{-1}$ .

the emission stretches again to the west with the increase of velocities. Finally, the emission moves back to the east around  $66 \text{ km s}^{-1}$ . The lack of the CS emission west of d2 around  $62 \text{ km s}^{-1}$  and the two westward extensions of CS emission at  $59 \text{ km s}^{-1}$  and  $64 \text{ km s}^{-1}$  define a hole in a position-velocity plot. Figure 12 illustrates this point clearly. In the position-velocity plot, the CS emission around [position, velocity] =  $[-6'' \sim -20'', 50 \sim 68 \text{ km s}^{-1}]$  delineates a shell structure. The small north-south extension of the CS emission prevents us from examining the velocity structure in that direction.

The structure of the CS shell in Figure 12 agrees well with that in  $\text{NH}_3$  (see gray scales in Fig. 12). Based on the mass and temperature in the shell, Zhang & Ho (1995) proposed that the structure in  $\text{NH}_3$  represents the swept-up material in an outflow. The  $\text{NH}_3$  (3, 3) maser, located at the extreme blueshifted velocities, is likely excited at the interface of the outflowing gas and the ambient material. The CS emission confirms the structure and kinematics observed in  $\text{NH}_3$ . It has been suggested that W51d2 is the driving source of the expanding shell (Zhang & Ho 1995).

3.4. Temperature Estimates from  $\text{CH}_3\text{CN}$

$\text{CH}_3\text{CN}$  traces high-density gas ( $n \sim 10^5 \text{ cm}^{-3}$ ) and, in some circumstances, provides good estimates of gas temperatures. We use the method of rotational diagrams to derive gas temperatures (see Hollis 1982; Loren & Mundy 1984; Olmi, Cesaroni, & Walmsley 1993). The details are

presented in Appendix B. In its basic form, we assume LTE and optically thin emission. Therefore, the level populations, which are then directly proportional to the line intensities of the  $K$  components, are translated to a single temperature via the Boltzmann equation (see eq. [B6]).

We fit Gaussian profiles to the  $\text{CH}_3\text{CN}$  spectra to derive intensities for all the components by minimizing the overall  $\chi^2$ . To reduce the number of free parameters, we assume that all the  $K$  components have the same line width. We further fix the frequency spacings of the different  $K$  components to the values listed in Table 3. For  $K \geq 4$ , the underlying hyperfine components are split by more than  $0.6 \text{ km s}^{-1}$ , the spectral resolution of the observations. They are therefore treated as separate components with relative intensities fixed to the relative strengths given in Table 3. Thus, the only free parameters are the line intensities of different  $K$  components and the  $V_{\text{LSR}}$  of the core. Figure 13 shows the comparison of the  $\text{CH}_3\text{CN}$  spectrum from e2 and the fit. The discrepancy at  $K = 5$  is probably due to the confusion by an unidentified line. The fitted intensities of the different  $K$  components and  $V_{\text{LSR}}$  are given in Table 2.

Figure 14 presents the rotational diagrams corresponding to the spectra from the positions of e2, e8, and W51-North: dust. The least-squares fit to all the components using equation (B6) gives rotational temperatures of  $140 \pm 30$ ,  $130 \pm 30$ , and  $200 \pm 60 \text{ K}$  for the e2, e8, and W51-North:dust cores, respectively. The intercept of the least-squares fit yields corresponding  $\text{CH}_3\text{CN}$  column densities of  $2.8 \times 10^{14}$ ,  $2.0 \times 10^{14}$ , and  $1.9 \times 10^{14} \text{ cm}^{-2}$ .

TABLE 2  
 $\text{CH}_3\text{CN}$  (8–7) LINE PARAMETERS

SOURCE	$V_{\text{LSR}}$ ( $\text{km s}^{-1}$ )	INTENSITY FOR $K$ COMPONENTS (kelvins)							
		$K = 0$	$K = 1$	$K = 2$	$K = 3$	$K = 4$	$K = 5$	$K = 6$	$K = 7$
W51e2 .....	55	24.7	29.5	30.8	33.4	22.2	18.1	13.7	3.8
W51e8 .....	59	32.4	12.3	25.1	27.0	17.5	11.5	10.7	2.7
W51-North:dust .....	60	14.1	14.0	16.3	19.8	10.2	8.0	7.9	3.0

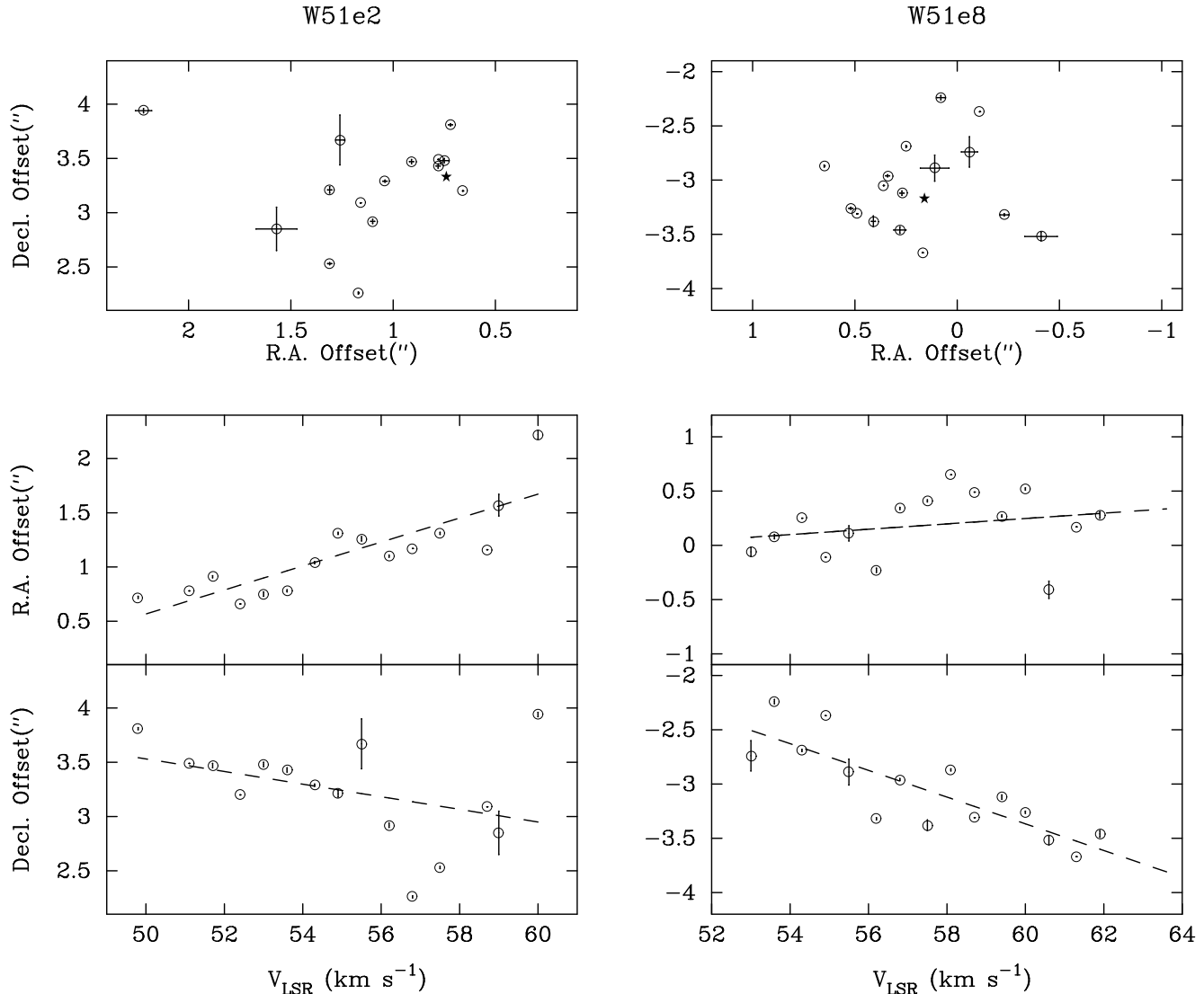


FIG. 11.—*Top*: Centroid positions of the  $\text{CH}_3\text{CN}$  ( $8_3-7_3$ ) emission measured from different velocity channels toward the e2 and e8 cores. The position is offset from the phase center at  $\alpha(1950) = 19^{\text{h}}21^{\text{m}}26^{\text{s}}.2$  and  $\delta(1950) = 14^{\circ}24'38''$ . The error bar is the  $1\sigma$  uncertainty from the elliptical Gaussian fitting. The positions of the continuum source e2 and e8 are labeled as a star. *Middle*: Right ascension offset of the emission centroid against the velocity of each channel. *Bottom*: the declination offset of the centroid against the velocity of each channel. The dashed lines are the least-squares fit.

When transitions of the lower  $K$  states become optically thick, the column density obtained in this formulation represents only the lower limit. Detection of both the  $\text{CH}_3\text{CN}$  and  $\text{CH}_3^{13}\text{CN}$  ( $8-7$ ) lines allows us to estimate the optical depth of the transitions. Assuming a  $^{12}\text{C}$  to  $^{13}\text{C}$  ratio of 40, we obtained an optical depth for the  $K = 0$  component of  $\text{CH}_3\text{CN}$  of about 2 for the e2, e8, and W51-North cores. This means that the level population for the  $K = 0$  is underestimated by a factor of  $\tau/(1 - e^{-\tau})$ , i.e., a factor of 2.3.

In Figure 14, it appears that the points corresponding to the  $K = 0$  and 1 components tend to lie on the upper side of the fit. Corrections for optical depth will move these points to even higher values. Therefore, the rotational temperatures derived from the lower  $K$  components will be smaller. Since the lower  $K$  components, with larger optical depths and lower energy levels, are likely excited in the outer regions of a core, the slope change in Figure 14 indicates a temperature increase toward the center of these cores. This is also seen in Figure 4 where the  $\text{CH}_3\text{CN}$  emission of the lower  $K$  components shows more extended

structures than those of the higher  $K$  components. A fit to the  $K \leq 3$  components yields rotational temperatures of 40 K for the e2, e8, and W51-North cores, respectively. These are similar to the values derived from  $\text{NH}_3$  (Zhang & Ho 1997).

#### 4. DISCUSSION

##### 4.1. Infall Speed

The CS is much more optically thick than the  $\text{CH}_3\text{CN}$  lines and, therefore, traces different regions in the molecular cloud than  $\text{CH}_3\text{CN}$  does. Compared with the  $\text{NH}_3$  maps of the region (Zhang & Ho 1997), the CS emission of the e2 and e8 cores is more extended, while the high  $K$  components of the  $\text{CH}_3\text{CN}$  emission are more compact. This is consistent with the fact that the high  $K$  components of  $\text{CH}_3\text{CN}$  samples much higher temperatures. Those lines, being sensitive to different regions in the cloud, allow us to examine qualitatively the variation of infall speed throughout the collapse region. The blueshifted emission peak and

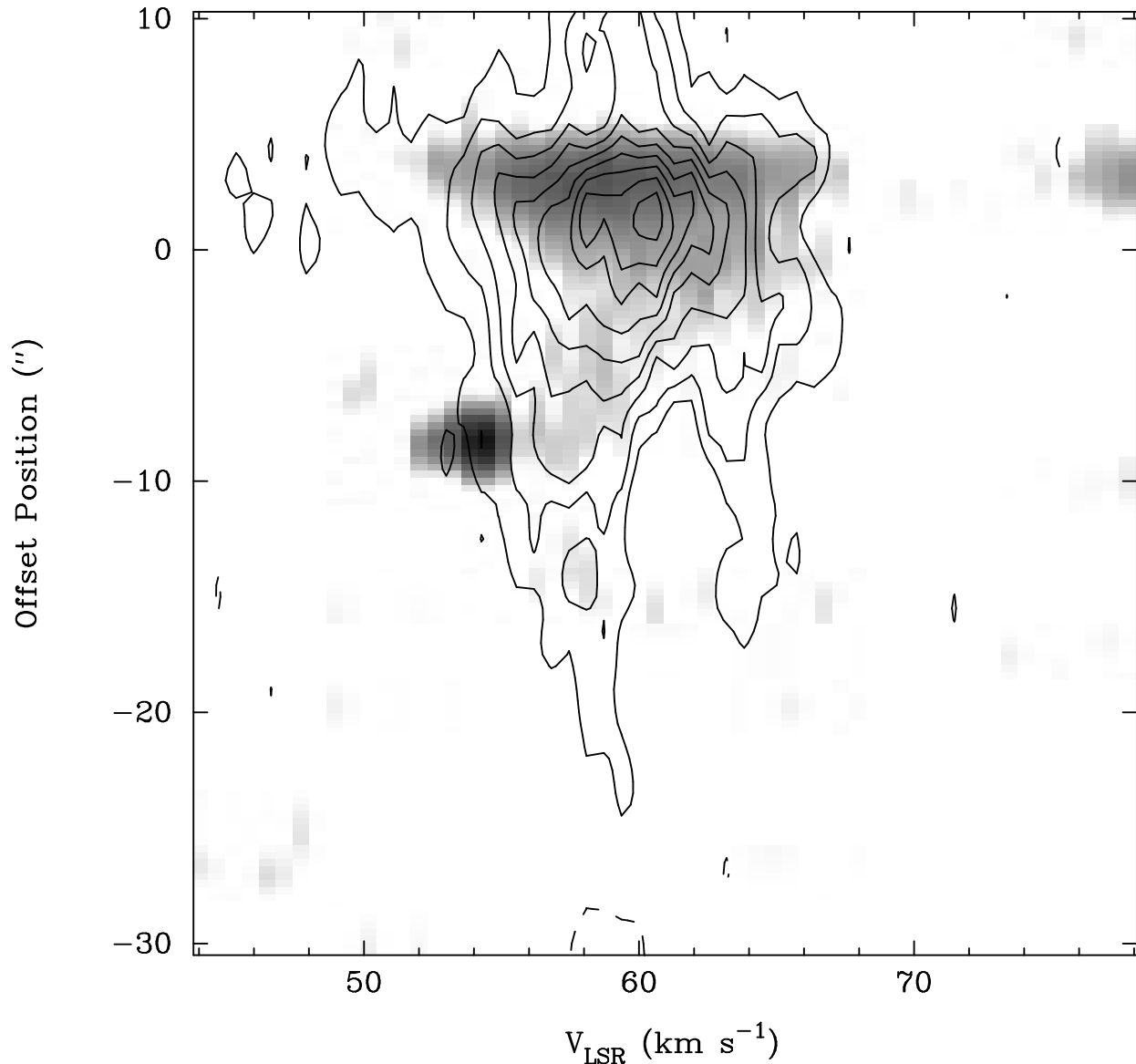


FIG. 12.—Position-velocity diagram toward W51-North. The cut along the right ascension is offset from the UC H II d2 at  $\alpha(1950) = 19^{\text{h}}21^{\text{m}}22^{\text{s}}.17$  and  $\delta(1950) = 14^{\circ}25'11''.9$ . The positive offset corresponds to the east. The contours are the CS (3–2) line, which is plotted at 1 Jy per  $3''.5$  beam intervals starting at 1 Jy per  $3''.5$  beam. The gray image is the  $\text{NH}_3$  (3,3) emission from Zhang & Ho (1995), which is plotted in logarithmic scales from 0.004 to 0.16 mJy per  $1''.5$  beam. The compact emission in  $\text{NH}_3$  at [position, velocity] =  $[-8.3'', 54.3 \text{ km s}^{-1}]$  is the (3, 3) maser.

the redshifted absorbing dip in the CS spectrum give an estimate of the infall speed of  $3.5 \text{ km s}^{-1}$  for both e2 and e8 cores. The more optically thin  $\text{CH}_3\text{CN}$  lines have a FWHM of about  $7 \text{ km s}^{-1}$ . If this line width is mainly attributed to infall motions, we can also derive an infall speed of  $3.5 \text{ km s}^{-1}$ . This is consistent with the  $\text{NH}_3$  estimate by Zhang & Ho (1997), who concluded that the infall motion is nearly constant throughout the infall zone. Note that the CS emission shows broader line width than  $\text{CH}_3\text{CN}$  owing to larger opacity.

In low-mass regions like L1527 (Ohashi et al. 1997), higher infall velocities are detected toward the inner part of the core. Typically, the mass of the circumstellar material around the embedded low-mass stars is comparable to the mass of the star. In such cases, the gravity of the central star is dynamically important to the infall motions in the envelope. On the other hand, the core mass around W51e2

is a few hundred solar masses, which is 1 order of magnitude larger than the mass of the central star. Therefore, the dynamics in the outer envelope is mainly determined by the mass distribution in the core. The constant infall around e2 and e8 is consistent with the  $r^{-2}$  density distribution (Zhang & Ho 1997) in the two cores.

#### 4.2. Rotation

The rotational axes for the e2 and e8 cores are at  $\text{P.A.} = 20^\circ \pm 17^\circ$  and  $\text{P.A.} = 66^\circ \pm 27^\circ$ , respectively. Although the inclination of the axes along the line of sight is not known, their projection on the plane of sky differs by  $46^\circ$ . This difference is larger than the  $1 \sigma$  error bars in the position angle. Judging from the fitting in Figure 11, we caution that the error in the position angle could be potentially larger. However, if the difference in the position angle is significant, this may have interesting implications. The

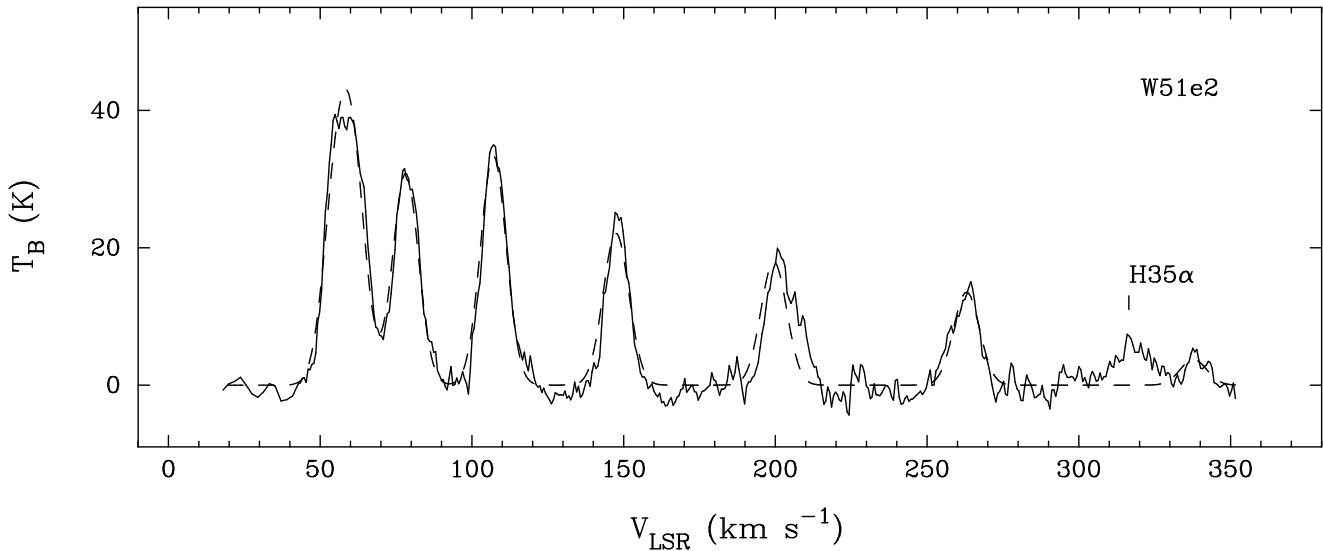


FIG. 13.—The  $\text{CH}_3\text{CN}$  (8–7) spectrum at the position of W51e2. The solid line is the observed spectrum. The dashed line is the fit of Gaussian components to the data.

dominant velocity gradient in the e1/e2 region at  $\sim 1'$  (2.4 pc) scales is in the north-south direction (Ho & Young 1996). If the e2 and e8 cores derive from fragmentations of the same parental cloud, our findings indicate that the axis of rotation is not preserved during cloud fragmentation. In the case of the e1/e2 region, the large angular momentum in the parental cloud is probably redistributed in terms of the relative motions of the e2 and e8 cores, i.e., the  $3 \text{ km s}^{-1}$  velocity differential between the two dense cores. The rotational axis of individual cores, on the other hand, is probably determined by internal dynamical interactions during fragmentation and may not follow the rotation of the parental cloud. The rotational axis of dense cores is apparently maintained, however, once the dense core is formed, as suggested by the spin-up motions in the e2 core.

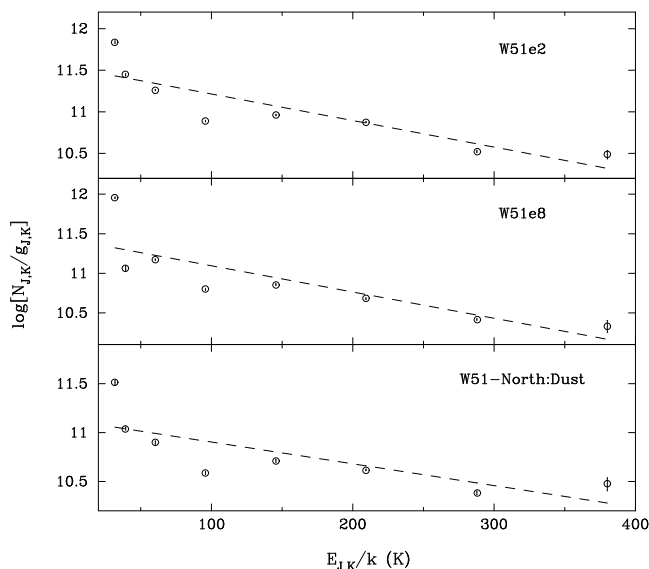


FIG. 14.—LTE rotational diagram of the  $\text{CH}_3\text{CN}$  (8–7) line. The dashed lines are the least-squares fits to all the  $K$  components using equation (B6).

#### 4.3. Is Infall Asymmetry due to Missing Flux in Interferometric Maps?

Each antenna pair in an interferometer measures a discrete Fourier component in the source. Only a finite number of Fourier components are synthesized in an observation. Because adjacent antennas cannot be stationed closer than the dish diameter without shadowing, very extended source emission is not sampled. If the source is dominated by extended emission, this effect makes the total flux in an interferometric map much lower than the measurement from a single dish radio telescope. When the extended emission lies at the cloud systemic velocity, this effect can produce false self-absorption.

Could the infall asymmetry seen toward e2 and e8 be due to missing large-scale structures at some particular velocities? Figure 7 indicates that this is not the case. We note that except for the CS, all line emissions are compact. In the case of CS, negative emissions exist from 48 to  $60 \text{ km s}^{-1}$ , indicating the presence of some extended structures. However, the CS spectrum  $9''$  north of e2 shows a symmetric line profile. If the missing extended emission produced the dip in the CS spectrum toward e2 around  $57 \text{ km s}^{-1}$ , the same effect would have given rise to a dip in the CS spectrum  $9''$  north of e2. The same reasoning also argues for the infall asymmetry toward e8. The absorption dip in CS toward the e8 core appears at a different velocity from that of e2, although the e8 core is only less than  $10''$  south of e2.

#### 4.4. Hot Cores Surrounding UC H II Regions

Compared with CS in the W51 region, the  $\text{CH}_3\text{CN}$  emissions are compact and closely associated with the 2 mm dust emission and the UC H II regions. The rotational temperatures in the W51 cores estimated from the high  $K$  components of the  $\text{CH}_3\text{CN}$  (8–7) are more than 100 K, similar to those hot cores in Orion and other H II regions. The lower  $K$  components give a rotational temperature of about 40 K, in agreement with the estimates from  $\text{NH}_3$  (1, 1) and (2, 2) (Zhang & Ho 1997). It is likely that the  $\text{NH}_3$  and the lower  $K$  components of  $\text{CH}_3\text{CN}$  trace only the cooler part



of the molecular core surrounding the H II region. Observations of other high-mass, star-forming regions have shown that CH<sub>3</sub>CN cores often do not coincide with the extended, evolved H II regions but arise from faint UC H II regions in the neighborhood of H<sub>2</sub>O masers (see, e.g., Hofner et al. 1996). Our data are consistent with this picture and confirm the suggestion that CH<sub>3</sub>CN is a good tracer of the early phase of OB star formation.

#### 4.5. RRL Emission from H II Regions

##### 4.5.1. Unusually Narrow RRL toward UC H II Region e2

The H35 $\alpha$  RRL emission is detected toward the UC H II region e2 and IRS 2 (also referred to as W51d in the centimeter wave radio continuum). The FWHM of the RRL toward the IRS 2 region ranges from 25 to 29 km s<sup>-1</sup> with typical fitting errors of 1 to 2 km s<sup>-1</sup>. High-resolution (a few arcseconds) observations of H76 $\alpha$  and H92 $\alpha$  have been made toward the same region by Garay, Reid, & Moran (1986) and by Mehringer (1994), respectively. The line width of the H76 $\alpha$  is about 27 km s<sup>-1</sup>, in agreement with the measurements of the H35 $\alpha$  line. The H92 $\alpha$  lines in the same region are  $\sim 32$  km s<sup>-1</sup> in width, much broader than the H35 $\alpha$  line. The centroid velocities of these lines are around 59 km s<sup>-1</sup>, suggesting that all the emissions are from the same region.

The broader H92 $\alpha$  line toward IRS 2 can be accounted for at least partly by pressure broadening, which is very sensitive to the quantum number,  $n$ , of the upper energy level of the RRL. The ratio of the Lorentzian width,  $\Delta V_L$ , to the Doppler width,  $\Delta V_D$ , for  $\alpha$  lines is given by (see Brocklehurst & Seaton 1972)

$$\frac{\Delta V_L}{\Delta V_D} = 0.14 \left( \frac{n}{100} \right)^{7.4} \left( \frac{10^4 \text{ K}}{T_e} \right)^{0.1} \left( \frac{n_e}{10^4 \text{ cm}^{-3}} \right) \left( \frac{2 \times 10^4 \text{ K}}{T_D} \right), \quad (1)$$

where  $n_e$  is the electron density and  $T_e$  is the electron temperature.  $T_D$  is the Doppler temperature, which is defined as

$$\Delta V_D = \sqrt{\frac{2(\ln 2)kT_D}{m}}, \quad (2)$$

where  $k$  and  $m$  are Boltzmann's constant and the mass of the ionized atom, respectively.

Assuming that  $\Delta V_D$  is equal to the H35 $\alpha$  line width, we find  $\Delta V_L/\Delta V_D$  ratio of 0.2 for H92 $\alpha$  and 0.05 for H76 $\alpha$ , for values of  $n_e = 2.3 \times 10^4 \text{ cm}^{-3}$  and  $T_e = 7700 \text{ K}$  (Mehringer 1994). According to Allen (1976), the total line width combining the Doppler and Lorentzian widths can be estimated via

$$\Delta V_T = \left[ \left( \frac{\Delta V_L}{2} \right)^2 + \Delta V_D \right]^{1/2} + \frac{\Delta V_L}{2}. \quad (3)$$

Applying the formula, we find a 10% increase upon the Doppler line width for H92 $\alpha$ . Since the Lorentzian width is directly proportional to electron densities, the contribution of pressure broadening can be larger if  $n_e$  increases.

Figure 15 shows the H35 $\alpha$  spectrum toward the UC H II region e2. The line is blended in the wings with transitions from other molecules, which raises the baseline of the spectrum. The FWHM of H35 $\alpha$  toward the UC H II region e2 is

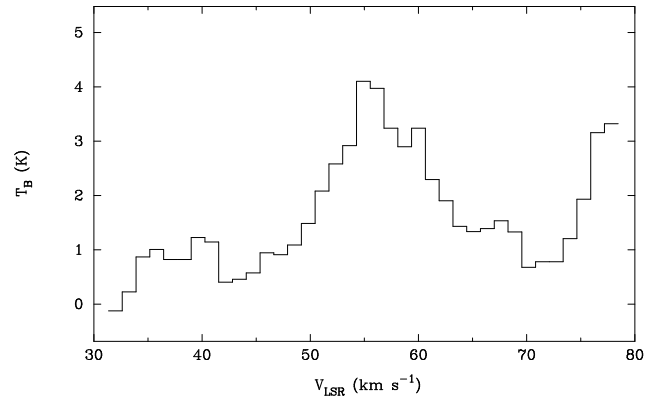


FIG. 15.—H35 $\alpha$  line profile from the position of e2. The line is smoothed with a 4'' beam. The emission at greater than 75 km s<sup>-1</sup> is the CH<sub>3</sub>CN (8–7)  $K = 7$  component. The baseline level is above zero because of line blending.

$13.5 \pm 1 \text{ km s}^{-1}$ , corresponding to an electron temperature of only  $4.0 \times 10^3 \pm 600 \text{ K}$  if the line width is solely attributed to thermal broadening. This line width is significantly narrower than the typical RRL width of more than 25 km s<sup>-1</sup> in the W51 region. For example, the H92 $\alpha$  line toward the UC H II region e1 has a FWHM of 27 km s<sup>-1</sup> (Mehringer 1994).

There have been few H II regions known so far to have narrow hydrogen RRL lines (e.g., G0.6–0.6; Planesas et al. 1991). In addition, these regions are normally extended and thought to have high metal abundances, which make radiative cooling more effective. Even in those cases, the narrowest line width reported in the literature is 14.4 km s<sup>-1</sup>, which was detected by Planesas et al. (1991) in H110 $\alpha$ .

W51e2 differs from the other narrow RRL H II regions not only for its narrower line width, but also for its compactness ( $\sim 2000 \text{ AU}$  in diameter) and high emission measure ( $1.5 \times 10^9 \text{ pc cm}^{-6}$ ). It is unlikely that the metal abundance in e2 is unusually high, since the rest of the W51 region has electron temperatures greater than 5000 K, with typical values around 7800 K. The UC H II region e1, which is likely associated with the same molecular cloud in which e2 is embedded, has an electron temperature of 8300 K.

The unusually narrow line width of H35 $\alpha$  allows us to set limits on the expansion velocity of the H II region e2. Once an H II region is developed, one should expect macro-turbulence and expansions of the ionized gas due to thermal pressure. For an uniformly expanding sphere of radial velocity  $V_{\text{exp}}$ , the profile function of the emergent radiation is the combination of two step functions,  $\theta(V + V_{\text{exp}}) - \theta(V - V_{\text{exp}})$ , if the emission is optically thin. When the expansion velocity is smaller than the Doppler line width, the total FWHM of an optically thin line from an expanding sphere is  $2V_{\text{exp}} + \Delta V_D$  (Sams, Moran, & Reid 1996). Assuming a minimal temperature of 3000 K for a fully ionized H II region, we find  $V_{\text{exp}} < 0.9 \text{ km s}^{-1}$ . This limit does not rule out macro-turbulent velocity (which adds quadratically with the thermal broadening) of a few kilometers per second.

Our observations provide direct evidence that the UC H II region e2 is not in notable expansion. Wood & Churchwell (1989) argued, based on a centimeter continuum survey, that the UC H II regions live much longer than

expected from free expansion. This motivated various proposals of confinement mechanisms. The coincidence of non-expansion of the H II region and infall of molecular gas around it strongly suggests that the collapse of molecular gas can be a viable mechanism preventing the H II region from expanding. Zhang & Ho (1997) computed the infall pressure and concluded that it is comparable to the thermal pressure in the H II region. This idea of infall confinement has been proposed in the study of W3(OH) (Reid et al. 1981) and G10.6 (Ho & Haschick 1986).

It is also peculiar that UC H II region e2 has very small turbulent velocity compared with most of the other H II regions. Certainly for the other H II regions in W51, typical turbulent velocity is about  $15 \text{ km s}^{-1}$ . This phenomenon of unusually small turbulent velocity has been reported in H II regions with high metal abundances (Planesas et al. 1991). Because most of the studies of hydrogen RRL have been conducted at longer centimeter wavelengths, those H II regions with high emission measures like the UC H II region e2 are optically thick and would not have been detectable in RRL. High angular resolution observations of RRL will be fruitful in finding these regions but only at frequencies higher than 20 GHz, where the free-free continuum is likely to be optically thin.

#### 4.5.2. Estimate Free-Free Emission Flux from RRL

Electron temperatures can be estimated from ratios of free-free continuum to RRL intensity if both emissions are optically thin (see Roelfsema & Goss 1992). Garay et al. (1986) and Mehringer (1994) estimated electron temperatures based on H76 $\alpha$  and H92 $\alpha$ , respectively. The typical electron temperatures in the region are around 7800 K.

Given the electron temperatures, one may estimate the contribution of thermal free-free emission (see Roelfsema & Goss 1992) according to

$$F_{\text{ff}} = 1.4 \times 10^{-4} \left( \frac{T_e}{\text{K}} \right)^{1.15} \left( \frac{\nu}{\text{GHz}} \right)^{-1.1} \left( \frac{\Delta V_D}{\text{km s}^{-1}} \right) F_{\text{RRL}}, \quad (4)$$

where  $F_{\text{RRL}}$  and  $F_{\text{ff}}$  are intensities of the RRL and free-free continuum, respectively. At the emission peak of H35 $\alpha$  toward the IRS 2 region, where  $T_e = 7700 \text{ K}$ ,  $\Delta V_D = 26 \text{ km s}^{-1}$ ,  $F_{\text{RRL}} = 2.7 \text{ Jy per } 3''.7 \times 3''.3 \text{ beam}$ , we obtain  $F_{\text{ff}} = 1.2 \text{ Jy per } 3''.7 \times 3''.3 \text{ beam}$ . This is comparable to the  $1.3 \text{ Jy beam}^{-1}$  measured at 2 mm. Thus, most of the 2 mm continuum at the peak of H35 $\alpha$  arise from the free-free emission. Toward e2, where  $T_e = 4000 \text{ K}$ ,  $\Delta V_D = 13.5 \text{ km s}^{-1}$ ,  $F_{\text{RRL}} = 1.5 \text{ Jy per } 4'' \times 4'' \text{ beam}$ , we get  $F_{\text{ff}} = 0.15 \text{ Jy beam}^{-1}$  as compared to  $3.3 \text{ Jy per } 4'' \text{ beam}$  measured at 2 mm. The estimated free-free flux is in a rough agreement with the extrapolation in § 3.2.1. The dust emission dominates the 2 mm continuum in this case.

#### 4.6. CH<sub>3</sub>CN Abundances

The production of CH<sub>3</sub>CN is mainly through the radiative association reaction of the CH<sub>3</sub><sup>+</sup> ion and HCN. The CH<sub>3</sub>CN abundance can be significantly enhanced in regions where the HCN abundance is increased. From the H<sub>2</sub> column density inferred from NH<sub>3</sub> (Zhang & Ho 1997), we estimate CH<sub>3</sub>CN abundance to be about  $5 \times 10^{-10}$ . Alternatively, using the H<sub>2</sub> column density estimated from the dust emission yields a CH<sub>3</sub>CN abundance of about

$2 \times 10^{-10}$ . These estimates are similar to those in the OMC-1 and Sgr B2 regions. We note that the abundance estimates are highly uncertain because of uncertainties in the CH<sub>3</sub>CN and H<sub>2</sub> column densities.

#### 4.7. Is W51-North: Dust a Massive Protostar?

Toward W51-North, the coincidence of the dense NH<sub>3</sub> core, the H<sub>2</sub>O and OH maser activities, and the 2 mm dust emission indicate that W51-North:dust is a site of ongoing star formation. The source is not detected at 20  $\mu\text{m}$  because of heavy extinction (Genzel et al. 1982). The absence of an H II region, the bright dust emission, and the nondetection of molecular outflows suggest a very early evolutionary stage of massive stars, similar to G31.41 (Cesaroni et al. 1994), the TW object in W3(OH) (Wilner, Welch, & Foster 1995), and W33A (Rengarajan & Ho 1996; Peng 1995).

### 5. CONCLUSIONS

The main conclusions of this paper are as follows.

1. The CS, CH<sub>3</sub>CN, CH<sub>3</sub>OCH<sub>3</sub>, and HCOOCH<sub>3</sub> lines from the W51e2 and W51e8 cores show suppressed redshifted emission as compared with the blueshifted component of the line. The line asymmetry increases systematically toward transitions of higher optical depths. Furthermore, for the CS line, the asymmetry is more prominent at higher angular resolutions. This pattern strongly indicates that the redshifted emission arises from gas in the foreground of the star and the blueshifted emission arises from the gas behind the star. The velocity extent of the blueshifted and the redshifted gas is similar to that of NH<sub>3</sub>, confirming the interpretation earlier that the e2 and e8 cores are in a state of collapse.

2. A velocity gradient at  $\sim 1''$  scale is identified in the e2 and e8 cores. The axes of the gradient in both cores do not seem to be in the same direction, suggesting that the rotational axis in the parental cloud is not preserved in the process of fragmentation.

3. The CS and CH<sub>3</sub>CN emission reveal molecular clumps that resemble the NH<sub>3</sub> cores identified before. The CH<sub>3</sub>CN emission is much more compact and better associated with the UC H II regions than the CS. It is likely that the CH<sub>3</sub>CN emission traces the dense and hot cores in the immediate neighborhood of massive stars. The temperature derived from the higher  $K$  components of CH<sub>3</sub>CN is greater than 100 K.

4. We detected an unusually narrow H35 $\alpha$  line toward UC H II region e2. The line width is about  $13.5 \text{ km s}^{-1}$ , leading to an electron temperature less than  $4 \times 10^3 \text{ K}$  and an H II region expansion velocity of less than  $1 \text{ km s}^{-1}$ .

5. Strong dust emission is detected toward an extremely young source in W51-North, and the new 2 mm continuum source is located at the peak of the line emission. Without a detection of its counterpart at cm wavelengths, this source may represent a massive protostar.

6. The CS gas west of W51d2 forms a shell in the position-velocity diagram, suggesting an expanding envelope that is propelled by winds from the massive star d2.

We thank K.-I. Morita and staff at the Nobeyama Observatory for their help during the observations. Q. Z. is in debt to D. J. Wilner and E. A. Bergin for many enlightening discussions.

## APPENDIX A

## EXPECTED SIGNATURES FROM AN INFALLING CLOUD CORE

The expected spectroscopic signatures from collapsing clouds have been simulated by a number of investigators (see, e.g., Leung & Brown 1977; Anglada et al. 1987; Zhou 1992; Walker, Narayanan, & Boss 1994) through radiative transfer codes. The key characteristics, however, can be illustrated in the following simplified model (see also Zhou et al. 1993). We approximate the real cloud cores with a centrally condensed, symmetric sphere. The infall motion is assumed to increase inward toward an embedded compact continuum source at the cloud center. This source can be the dust continuum at millimeter or submillimeter wavelengths or an H II region embedded in high-mass cloud cores. Figure 16 shows the isocontours of the projected infall velocity along the line of sight. The emission at the redshifted velocity ( $V - V_{\text{LSR}}$ ) arises from the small volume of gas around R1 and R2 on the front side of the continuum source. Similarly, the emission at the blueshifted velocity,  $-(V - V_{\text{LSR}})$ , arises from B1 and B2 on the back side of the continuum source. Given the excitation temperatures,  $T$ , and optical depth,  $\tau$ , around positions 1 and 2, and the brightness temperature of the continuum source,  $T_{\text{cont}}$ , we have line intensities of the red component of

$$T_{\text{R}} = (T_2 - T_{\text{cont}})(1 - e^{-\tau_2})e^{-\tau_1} + (T_1 - T_{\text{cont}})(1 - e^{-\tau_1}). \quad (\text{A1})$$

Likewise, the blueshifted emission is given by

$$T_{\text{B}} = T_1(1 - e^{-\tau_1})e^{-\tau_2} + T_2(1 - e^{-\tau_2}). \quad (\text{A2})$$

Therefore, the difference between the blueshifted and redshifted emission follows as

$$T_{\text{B}} - T_{\text{R}} = T_{\text{cont}}[1 - e^{-(\tau_1 + \tau_2)}] + (T_2 - T_1)(1 - e^{-\tau_1})(1 - e^{-\tau_2}). \quad (\text{A3})$$

There are several cases that are worth discussing.

1. According to equation (A3),  $T_{\text{B}} \simeq T_{\text{R}}$  when  $\tau_1 \ll 1$  and  $\tau_2 \ll 1$ . The line is symmetric with respect to the cloud velocity when it is optically thin. This case is of particular interest in defining the systemic velocity of a cloud and can be used to test the existence of multiple cloud components. Within the telescope beam, if there are multiple cloud components that are displaced in velocity, one should expect to see multiple line components in an optically thin spectrum.

2. When the continuum source is absent and lines become optically thick, one expects  $T_{\text{B}} > T_{\text{R}}$  if  $T_2 > T_1$  according to equation (A3). The latter condition is often satisfied in dense cores where temperatures and densities are centrally enhanced. This case shows that optically thick lines should appear asymmetric because of infall motions and increasing excitation toward the core center.

3. If the embedded continuum source is bright enough so that  $T_{\text{cont}} > T_1, T_2$ , then, according to equations (A1) and (A2), one finds  $T_{\text{R}} < 0$  and  $T_{\text{B}} > 0$ . In this case, the inverse P Cygni profiles provide a powerful diagnostic of infall, *independent of the excitation condition in the core and free of confusion from core rotation*.

4. Even if  $T_{\text{cont}} < T_1, T_2$ , based on equation (A3), one expects to find an increase of line asymmetry with the increase of  $T_{\text{cont}}$ . The application of this case is as follows: The continuum emission is often more centrally condensed than the line emission, especially in the situation of UC H II regions. Thus, the brightness temperature of the continuum should rise faster than the line temperature when the source is observed with finer angular resolutions. By mapping emission with different angular resolutions, one can test if the change in line asymmetry is consistent with infall onto a continuum source.

To summarize, good infall evidence should consist of the following characteristics:

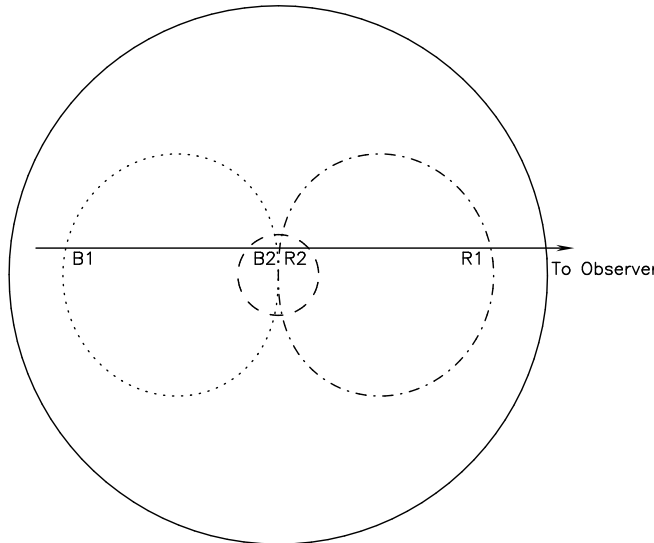


FIG. 16.—A schematic model of an infalling cloud adopted from Zhou et al. (1993). The isoprojected velocities along the line of sight are shown in dash-dotted (redshifted velocities) and dotted (blueshifted velocities) lines. The dashed circle denotes the continuum source.

1. Symmetric line profiles with respect to the cloud systemic velocity in optically thin transitions. This is a powerful test against the possibility of unrelated multiple cloud components.
2. When transitions become optically thick, the line profiles turn asymmetric with respect to the cloud systemic velocity, with the blue component stronger than the red component. This asymmetry increases toward lines of larger optical depths.
3. If the infall velocity increases inward, the line widths of higher excitation lines become broader.
4. The existence of an embedded compact continuum source will enhance line asymmetries. The enhancement of asymmetry depends on the contrast between the continuum and gas temperatures. If the compact continuum source is more centrally condensed than the gas emission, one expects to see more pronounced line asymmetry at higher angular resolutions.
5. The lines show the inverse P Cygni profiles when the continuum temperature exceeds the gas temperature.
6. If infall motion is radial, one expects to see the change of the projected infall velocity along the line of sight across the core.

## APPENDIX B

### CH<sub>3</sub>CN MOLECULE

Rotational levels of the symmetric top molecule CH<sub>3</sub>CN are characterized by two quantum numbers, i.e., the total angular momentum,  $J$ , and the projection of  $J$  on the symmetry axis of the molecule  $K$  (see Boucher et al. 1980 for a detailed discussion). Since there is no dipole moment perpendicular to the symmetry axis, the dipole selection rules only allow radiative transitions between levels of the two adjacent  $J$  with the same  $K$ . The energy difference between the two adjacent  $J$  levels is nearly independent of  $K$ . This property makes all the  $K$  transitions from  $J$  to  $J - 1$  closely spaced in frequency and easy to observe in the same frequency band of a telescope. Each successive  $K$  component is shifted in frequency owing to the centrifugal distortion.

CH<sub>3</sub>CN has two distinct species, designated  $A$  and  $E$  for the different nuclear spin state. Rotational levels with  $K = 3n$ , where  $n$  is an integer, belong to the  $A$  species, and  $K \neq 3n$  levels belong to the  $E$  species. Since radiative transitions between the two species are prohibited and the number of collisional rates changing from one to the other is very small, the abundances of the states may not be equal.

Since the radiative process across the  $K$  ladders of the same  $J$  is forbidden, populations in different  $K$  components can provide a measure of temperature if the molecule in relevant levels is thermalized. A conventional treatment is to assume LTE and optically thin emission (Hollis 1982; Loren & Mundy 1984). In this case, the optical depth and thus the level populations are directly proportional to the line intensity. In general, the optical depth for each of the  $A$  and  $E$  species of the CH<sub>3</sub>CN components decreases toward higher  $K$  numbers as a result of decreasing populations toward higher excitation. However, except for the  $K = 0$  component, the  $A$  species have a nuclear spin statistical weight that is a factor of 2 larger than the  $E$  species. Therefore, the optical depth of the  $K = 3$  component can be larger than that of  $K = 2$ . For the conditions in W51, an large velocity gradient (LVG) calculation indicates that the opacity ranks in a decreasing order as  $K = 0, 1, 3, 2, 4, 5$ , and 6.

In the optically thin limit, the level population in the upper  $K$  level of the CH<sub>3</sub>CN  $J_K - (J - 1)_K$  transition is given by

$$N_{J,K} = \frac{3k(2J+1)}{8\pi^3\nu\mu S(J,K)} \int T_b dV. \quad (B1)$$

Here  $\nu$  is the line frequency of the  $J_K - (J - 1)_K$  transition,  $\mu = 3.91$  D is the dipole moment, and the line strength,

$$S(J,K) = \frac{J^2 - K^2}{J}, \quad (B2)$$

is given in Table 3.

Under the condition of thermal equilibrium, the level populations are related by a single temperature. Therefore,

$$N_{J,K} = \frac{g_{J,K}}{g_{K,K}} N_{K,K} \exp \left[ -\frac{E_{J,K} - E_{K,K}}{kT_{\text{rot}}} \right], \quad (B3)$$

where  $g_{J,K}$  is the statistical weight of the  $(J, K)$  level. Here  $g_{J,K} = (2J+1)g_K$ , and the nuclear spin statistical weight is (see Boucher et al. 1980)

$$g_K = \begin{cases} \frac{1}{3}(4I^2 + 4I + 3)(2I + 1), & \text{for } K = 0; \\ \frac{2}{3}(4I^2 + 4I + 3)(2I + 1), & \text{for } K = 3n, \text{ but not } 0; \\ \frac{2}{3}(4I^2 + 4I)(2I + 1), & \text{for } K \neq 3n, \end{cases} \quad (B4)$$

where  $I = \frac{1}{2}$  is the nuclear spin of hydrogen.

The  $N_{K,K}$  is described by the same temperature (see Loren & Mundy 1984; Olmi, Cesaroni, & Walmsley 1993 for a slightly different formulation) with respect to the ground level  $N_{0,0}$  through

$$N_{K,K} = \frac{g_{K,K}}{g_{0,0}} N_{0,0} \exp \left[ -\frac{E_{K,K}}{kT_{\text{rot}}} \right]. \quad (B5)$$

TABLE 3  
MOLECULAR PARAMETERS OF CH<sub>3</sub>CN (8–7)<sup>a</sup>

Transition $K^b$	$F'-F^c$	Frequency (GHz)	Line Strength	$E_u$ (K)
0 .....		147.174594	8.000	31.8
1 .....		147.171757	7.875	39.3
2 .....		147.163249	7.500	60.3
3 .....		147.149073	6.875	95.8
	7–6	147.149131	1.994	
	9–8	147.149128	2.574	
	8–7	147.148960	2.263	
4 .....		147.129135	6.000	145.6
	7–6	147.129351	1.734	
	9–8	147.129323	2.238	
	8–7	147.129033	1.968	
5 .....		147.103742	4.875	209.3
	7–6	147.103934	1.416	
	9–8	147.103873	1.828	
	8–7	147.103427	1.607	
6 .....		147.072650	3.500	287.8
	7–6	147.072889	1.012	
	9–8	147.073789	1.306	
	8–7	147.072152	1.148	
7 .....		147.035837	1.875	380.1
	7–6	147.036230	0.549	
	9–8	147.036083	0.709	
	8–7	147.035221	0.623	

<sup>a</sup> From Boucher et al. 1980.

<sup>b</sup> Projected angular momentum number of  $J$  on the symmetric axis.

<sup>c</sup> Total angular momentum quantum number including the nuclear spin.

Combining the above equations and converting to logarithmic form, we have

$$\ln \frac{N_{J,K}}{g_{J,K}} = \ln \frac{N_{\text{tot}}}{Q(T)} - \frac{E_{J,K}}{k} \frac{1}{T_{\text{rot}}} \quad (\text{B6})$$

Here the partition function

$$Q(T) = \sum_{J,K} g_{J,K} \exp \left[ - \frac{E_{J,K}}{kT_{\text{rot}}} \right], \quad (\text{B7})$$

and  $N_{\text{tot}}$  is the total CH<sub>3</sub>CN number density in all rotational states. Therefore, given brightness temperatures of different  $K$  components, one may compute the level population,  $N_{J,K}$ , and derive  $T_{\text{rot}}$  and the total column density  $N_{\text{tot}}$ . Studies by Wilner, Wright, & Plambeck (1994) show that  $T_{\text{rot}}$  derived in this formulation agrees well with those from the LVG calculations.

#### REFERENCES

- Allen, C. W. 1976, *Astrophysical Quantities* (London: Athlone Press)
- Anglada, G., Rodríguez, L. F., Cantó, J., Estella, R., & López, R. 1987, *A&A*, 186, 280
- Bieging, J. 1975, in *H II region and related Topics*, ed. T. L. Wilson & D. Downes (Berlin: Springer), 443
- Boucher, D., Burie, J., Dubrulle, A., & Demaison, J. 1980, *J. Phys. Chem. Ref. Data*, 9, 659
- Brocklehurst, M., & Seaton, M. J. 1972, *MNRAS*, 157, 179
- Cesaroni, R., Olmi, L., Walmsley, C. M., Churchwell, E., & Hofner, P. 1994, *ApJ*, 435, L137
- Garay, G., Reid, M. J., & Moran, J. M. 1986, *ApJ*, 289, 681
- Gaume, R. A., Johnston, K. J., & Wilson, T. L. 1993, *ApJ*, 417, 645
- Gaume, R. A., & Mutel, R. 1987, *ApJS*, 65, 193
- Genzel, R., Becklin, E. E., Wynn-William, C. G., Moran, J. M., Reid, M. J., Jaffe, D. J., & Downes, D. 1982, *ApJ*, 255, 527
- Genzel, R., & Downes, D. 1977, *A&AS*, 30, 145
- Hofner, P., Kurtz, S., Churchwell, E., Walmsley, C. M., & Cesaroni, R. 1996, *ApJ*, 460, 359
- Hollis, J. M. 1982, *ApJ*, 260, 159
- Ho, P. T. P., Genzel, R., & Das, A. 1983, *ApJ*, 266, 596
- Ho, P. T. P., & Haschick, A. D. 1986, *ApJ*, 304, 501
- Ho, P. T. P., & Young, L. M. 1996, *ApJ*, 472, 742
- Leung, C. M., & Brown, H. S. 1977, *ApJ*, 214, L73
- Loren, B. L., & Mundy, L. G. 1984, *ApJ*, 286, 232
- Lovas, F. J. 1992, *J. Phys. Chem. Ref. Data*, 21, 181
- Mehringer, D. M. 1994, *ApJS*, 91, 713
- Martín-Pintado, J., Bachiller, R., Thum, C., & Walmsley, M. 1989, *A&A*, 215, L13
- Olmi, L., Cesaroni, R., & Walmsley, C. M. 1993, *A&A*, 307, 599
- Ohashi, N., Hayashi, M., Ho, P. T. P., & Momose, M. 1997, *ApJ*, 475, 211
- Planesas, P., Gómez-González, J., Rodríguez, L. F., & Cantó, J. 1991, *Rev. Mexicana Astron. Astrof.*, 22, 19
- Peng, Y. 1995, Ph.D. thesis, University of Maryland
- Reid, M. J., Haschick, A. D., Burke, B. F., Moran, J. M., Johnston, K. J., & Swenson, G. W., Jr. 1981, *ApJ*, 239, 89
- Reid, M. J., Schneps, M. H., Moran, J. M., Gwinn, C. R., Genzel, R., Downes, D., & Rönnäng, R. 1988, *ApJ*, 330, 809
- Rengarajan, T. N., & Ho, P. T. P. 1996, 465, 363
- Roelfsema, P. R., & Goss, W. M. 1992, *A&A Rev.*, 4, 161
- Rudolph, A., Welch, W. J., Palmer, P., & Dubrulle, R. 1990, *ApJ*, 363, 528
- Sams, B. J., III, Moran, J. M., & Reid, M. J. 1996, *ApJ*, 459, 623
- Scott, P. F. 1978, *MNRAS*, 183, 435
- Walker, C. K., Narayanan, G., & Boss, A. P. 1994, *ApJ*, 431, 767
- Wood, D. O. S., & Churchwell, E. 1989, *ApJS*, 69, 831
- Wilner, D. J., Welch, W. J., & Foster, J. R. 1995, *ApJ*, 449, L73
- Wilner, D. J., Wright, M. C. H., & Plambeck, R. L. 1994, *ApJ*, 422, 642
- Zhang, Q., & Ho, P. T. P. 1995, *ApJ*, 450, L63
- , 1997, *ApJ*, 488, 241
- Zhou, S. 1992, *ApJ*, 394, 204
- Zhou, S., Evans, N. J., II, Butner, H. M., Kutner, M. L., Leung, C. M., & Mundy, L. G. 1990, *ApJ*, 363, 168
- Zhou, S., Evans, N. J., II, Kömpe, C., & Walmsley, C. M. 1993, *ApJ*, 404, 232

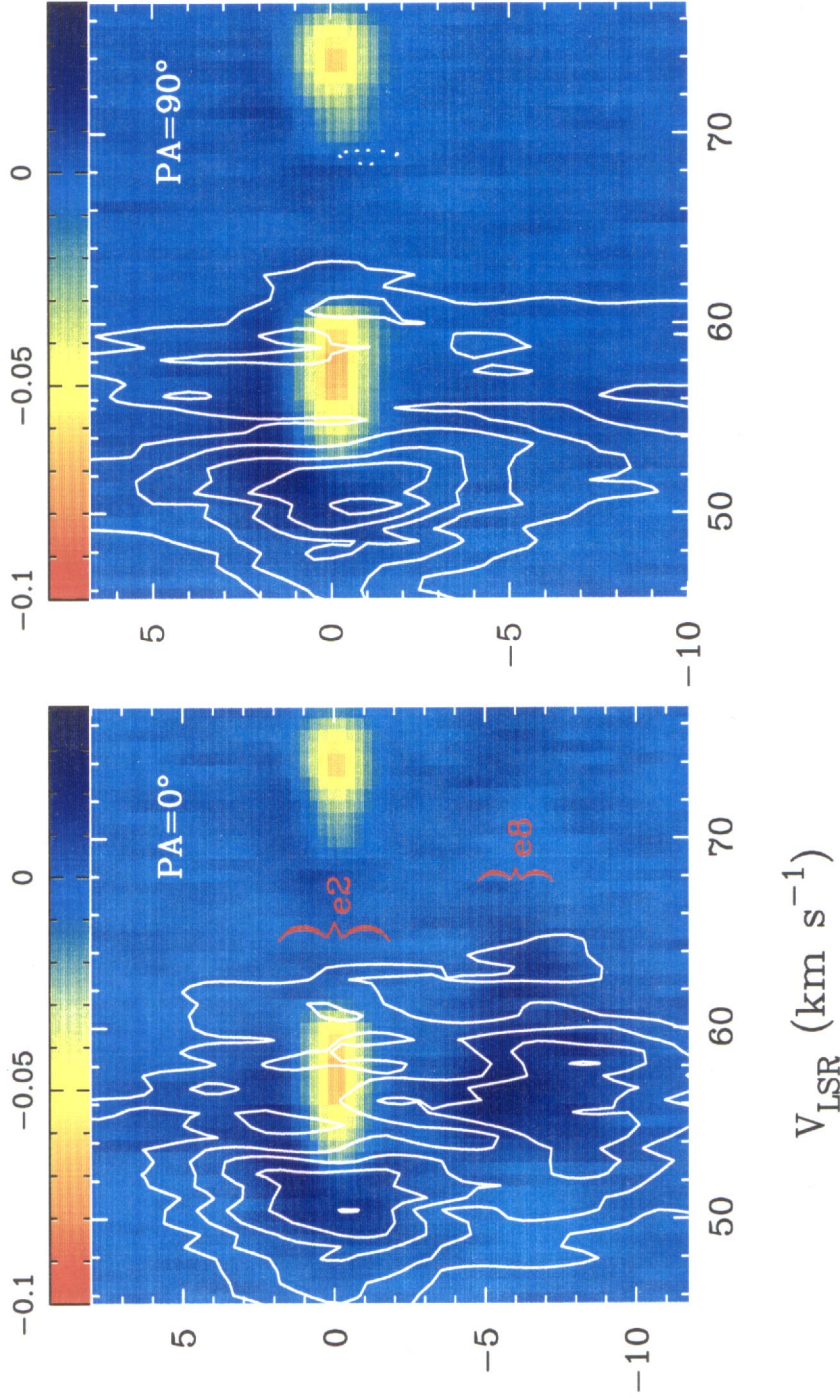


FIG. 10—Position-velocity diagram of the CS (3–2) line overlaid on that of the  $\text{NH}_3$  (2, 2) from Zhang & Ho (1997). The cut is offset from W51e2 at  $\alpha(1950) = 19^{\text{h}}21^{\text{m}}26^{\text{s}}.247$  and  $\delta(1950) = 14^{\circ}24'41''.3$  with position angles of  $0^\circ$  and  $90^\circ$ . The contours are the CS emission plotted at  $1.2 \text{ Jy beam}^{-1}$  interval starting from  $1.2 \text{ Jy beam}^{-1}$ . The color scales are the  $\text{NH}_3$  (2, 2) emission plotted from  $-0.1 \text{ Jy per } 1'' \text{ beam}$  to  $0.05 \text{ Jy per } 1'' \text{ beam}$ . Features near [position, velocity] = [ $0''$ ,  $75 \text{ km s}^{-1}$ ] are the first satellite hyperfine component of the  $\text{NH}_3$  (2, 2).

ZHANG, HO, & OHASHI (see 494, 645)